

## Two lithospheric profiles across southern California derived from gravity and seismic data

Tanya Romanyuk<sup>a,\*</sup>, Walter D. Mooney<sup>b</sup>, Shane Detweiler<sup>b</sup>

<sup>a</sup> *Institute of Physics of the Earth, B. Gruzinskaya 10, Moscow 123 810, Russia*

<sup>b</sup> *U.S. Geological Survey, MS 977, 345 Middlefield Road, Menlo Park, CA 94025, USA*

Received 30 September 2005; received in revised form 19 August 2006; accepted 18 September 2006

### Abstract

We present two detailed 2-D density transects for the crust and uppermost mantle across southern California using a linear gravity inversion technique. This technique parameterizes the crust and upper mantle as a set of blocks that are based on published geologic and seismic models. Each block can have a range of densities that are constrained where possible by borehole measurements, seismic velocities, and petrologic data. To further constrain the models, it is assumed that the lithosphere is close to isostatic equilibrium at both ends of the profiles, in the deep ocean and east of the Mojave Desert. We calculate the lithostatic pressure variations field for the whole cross section to rule out the geophysically insignificant solutions. In the linear equation,  $\rho = a + bV$  ( $V$ , seismic P-wave velocity;  $\rho$ , density), which approximates the mantle density–velocity ( $\rho$ – $V$ ) relationship, different coefficients for  $b$  were evaluated. Lower coefficients ( $b < 0.2$ ) correspond to an almost purely thermally perturbed mantle, while higher coefficients ( $b > 0.3$ ) imply that other effects, such as composition and/or metamorphic changes, play an important role in the mantle. Density models were constructed with the coefficient  $b$  ranging from 0 to 0.6. The results indicate that a high  $b$  value in the mantle  $\rho$ – $V$  relationship is associated with less dense crust in the Mojave block and more dense crust in the Catalina schist block. In the less dense Mojave block, the average density of the whole crust is  $\sim 2.75 \text{ g/cm}^3$ , while that of the lower crust is  $\sim 2.72 \text{ g/cm}^3$ . These densities imply a high silica content in the crust, and a minor fraction of basic rock in the lower crust, or perhaps the absence of a basaltic layer altogether. By comparison, the average density of a typical continental stable platform is  $\sim 2.85 \text{ g/cm}^3$ . Models with higher  $b$  coefficients (0.5–0.6) are characterized by a large isostatic imbalance. On the other hand, lower  $b$  values (0–0.2) require a consolidated whole crust density in the Mojave Desert of  $\sim 2.78 \text{ g/cm}^3$ , and a lower crust density of  $\sim 2.89 \text{ g/cm}^3$  with mostly basaltic composition. This contradicts the observed, lower  $V_p/V_s$ -ratio in the Mojave Desert associated with mostly felsic and low-density crust. Models with lower  $b$  coefficients (0.1–0.2) are characterized by an absence of local Airy compensation beneath the San Gabriel Mountains at the LARSE-1 profile. These, and other non-gravity arguments, suggest optimal solutions to the mantle  $\rho$ – $V$  relation of  $b \sim 0.2$ – $0.4$ . This, in turn, means that both thermal and petrological effects occur inside the downwelling of the uppermost mantle high velocity body located beneath the Transverse Ranges. During the development of this mantle downwelling, the basaltic layer of the Mojave block was likely eroded and pulled down into the high velocity body. Those basaltic fragments may have been transformed into eclogites, and this metamorphic change implies a higher  $b$ -coefficient density–velocity relationship than would be expected for a purely thermal process.

Published by Elsevier Ltd.

**Keywords:** Southern California; Gravity inversion; Density–seismic velocity relation

\* Corresponding author.

*E-mail addresses:* [t.romanyuk@relcom.ru](mailto:t.romanyuk@relcom.ru), [t.romanyuk@mail.ru](mailto:t.romanyuk@mail.ru), [romanyuk@ifz.ru](mailto:romanyuk@ifz.ru) (T. Romanyuk).

### 1. Introduction

Estimates of lithospheric densities are unreliable when they are based only on modeling the observed gravity field because of the intrinsic non-uniqueness of gravity data inversions. To enhance the accuracy of gravity models, a sufficient quantity of *a priori* seismic, geophysical, geological, and petrological constraints are needed. Also, stronger lateral density contrasts within both the crust and the mantle, and more pronounced depth undulations of density boundaries yield better conditions for density modeling. These conditions are satisfied in southern California, and we present modeled density profiles across the ocean–continent transition and the San Andreas fault plate transform boundary, the geophysics of which are already well studied.

The modeled profiles (Fig. 1a and b) cross the contrasting morphological structures of the southwestern North American plate. They begin in the abyssal plain of the Pacific Ocean, with water depth of ~4 km, and then cross the Patton escarpment, and the wide continental shelf (California Borderlands) where marine sedimentary basins alternate with ridges. On the continent, the profiles transect the deep Los Angeles, San Gabriel and San Fernando sedimentary basins, the uplifted thrust block of the San Gabriel and Pelona Mountains (~2800 m elevation), and finally terminate

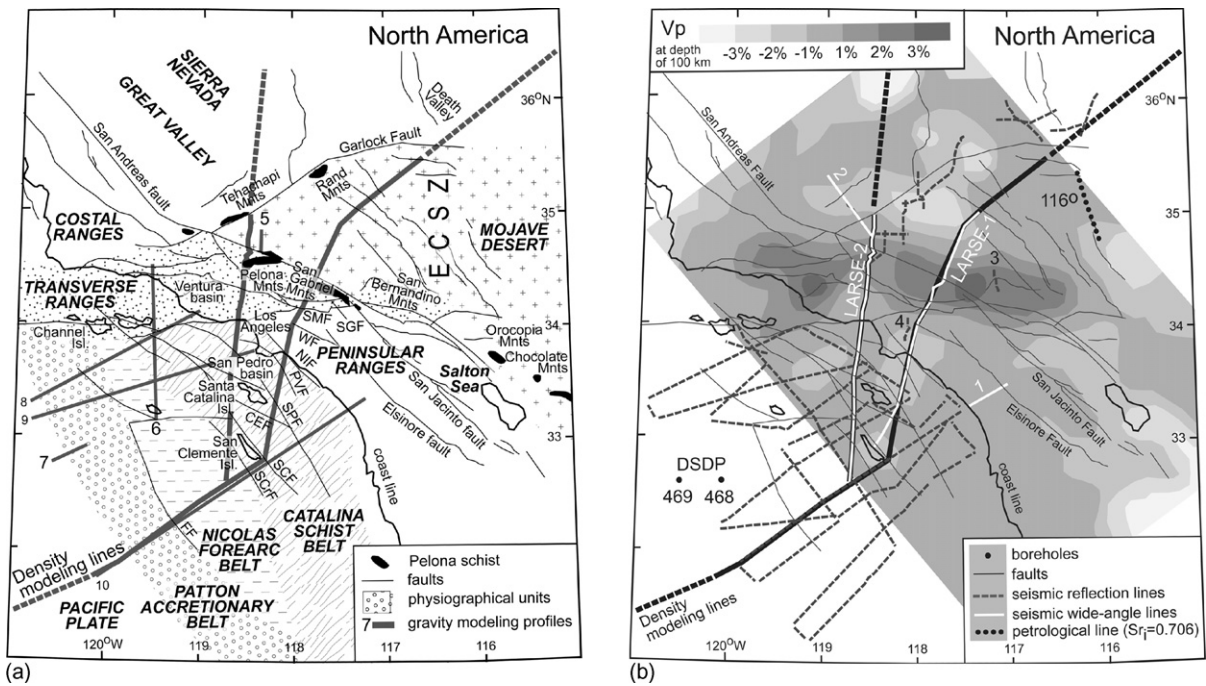


Fig. 1. (a) Simplified tectonic scheme of southern California showing physiographical units in different patterns and quaternary faults in black lines. The location of the gravity modeling profiles are shown in a thick gray line, whereas modeling profiles from literature are: (5) (Li et al., 1992a, the most southern COCORP segment), (6 and 7) (Keller and Prothero, 1987), (8–10) (Miller, 2002). Outcrops of the schists near Rand, Pelona, San Gabriel, Orocochia, and the Chocolate Mountains are shown in black. ECSZ indicates the Eastern California Shear Zone. Fault abbreviations: CEF: Catalina escarpment fault, FF: Ferrello fault, NIF: Newport Inglewood fault, PVF: Palos Verdes fault, ScRF: Santa Cruz Basin fault, SCF: San Clemente fault, SGF: San Gabriel fault, SPF: San Pedro Basin fault, WF: Whittier fault, SMF: Sierra Madre fault. (b) Map of southern California showing geophysical studies and locations of the gravity modeling profiles. Tomographic image of the upper-mantle seismic structure at 100 km depth from Humphreys and Clayton (1990) is shown in gray shading. The main long-range seismic experiments lines are: LARSE-1: [crustal and uppermost mantle models: onshore (Fuis et al., 2001; Zhu, 2000); upper mantle tomographic cross-section (Kohler, 1999); offshore (ten Brink et al., 2000)]; LARSE-2: [onshore (Fuis et al., 2003); offshore (ten Brink et al., 2000)]; COCORP (Cheadle et al., 1986)]. The minor short-range profiles are labeled by numbers: (1) (Li et al., 1993), (2) (Malin et al., 1995), (3) (Li et al., 1992b), (4) (Shaw and Shearer, 1999). The dotted black line in the Mojave Desert labeled as 116° marks the western edge of the North American mantle (Miller et al., 2000); geochemical signature of mafic rocks east of this line indicate an ancient Precambrian enriched lithosphere source, whereas rocks west of this line are derived from mantle with oceanic geochemical and isotopic signatures. The location of the Deep Sea Drilling Project and Ocean Drilling Project, Leg 63 site 468 (Patton escarpment) and site 469 (ocean to the west of the Patton escarpment) (Yeats et al., 1981; Yeats and Haq, 1981; Vedder et al., 1981) indicated by DSDP 469 and 468 are used to constrain the top of the oceanic crust of the Pacific plate, and the sediment thickness and densities on the Pacific plate and Patton escarpment.

in the Mojave Desert, a continental plateau standing  $\sim 700$  m above sea level. Beneath the surface, the profiles cross interesting uppermost-mantle features, including a high-velocity body beneath the Transverse Ranges at a depth of 200 km. Most of the profiles follow the LARSE-1 and LARSE-2 lines (Los Angeles Region Seismic Experiment—lines 1 and 2), where many seismic experiments have been performed during the past decade (Lutter et al., 1999, 2004; Fuis et al., 2001, 2003, 2004).

An investigation of the relation between seismic P-wave velocity and density is essential to constrain the physical state of the mantle. It has been shown that at a transform plate boundary with additional compression (i.e., a transpressional regime), mantle downwelling, and thrust-fold crustal complexes, such as the San Gabriel and San Bernardino Mountains, can develop (Humphreys and Hager, 1990; Pysklywec et al., 2000; Houseman et al., 2000; Billen and Houseman, 2004). The driving force of the process is thought to be gravity instability. Whether the density contrasts driving the system are due to a purely thermal process or to both thermal and petrological effects beneath southern California has not yet been established. Therefore, we attempt to estimate the  $b$ -coefficient of the linear velocity–density relation  $\rho = a + bV$  ( $V$ , seismic P-wave velocity;  $\rho$ , density) for the uppermost mantle down to 200 km depth beneath southern California by directly integrating the linear velocity–density relation in the density model. Lower coefficients ( $b < 0.2$ ) correspond to an almost purely thermally perturbed mantle, while higher coefficients ( $b > 0.3$ ) imply that other effects such as composition and/or metamorphic changes play an important role in the mantle (see Section 3.1, for more details).

The western edge of the Precambrian, North American cratonic lithosphere is believed to be located at  $\sim 116^\circ\text{W}$  in the central Mojave Desert (Fig. 1a) (Miller et al., 2000). The Miocene mafic rocks, west of  $116^\circ\text{W}$ , are presumably derived from mantle material that has an oceanic, geochemical, and isotopic signature. Therefore, we assume that at least the uppermost mantle along the profiles is of the same origin, and can be described by a common velocity–density ratio.

## 2. Data compilation to constrain the *a priori* density model

The gravity field of the ocean–continent transition in southern California is characterized by a steady decrease from about  $-22$  mGal free air anomalies over the Pacific plate, to negative Bouguer anomalies of about  $-120$  mGal over the Mojave Desert (Langenheim and Jachens, 1996; Wooley and Langenheim, 2001). Different borehole, geological, seismic data, and petrological constraints are compiled in the *a priori* seismic-geological models (Fig. 2). Those data are used to constrain the density models (Fig. 3). Taking into account the density–temperature relations (Tables 1 and 2) of Birch (1961) and Christensen and Mooney (1995), we construct *a priori* density limits (Table 3) for each block of the models.

Table 1  
Reducing densities versus temperature

Density (g/cm <sup>3</sup> )					
0 °C	200 °C (–0.018)	400 °C (–0.036)	600 °C (–0.054)	800 °C (–0.072)	1000 °C (–0.09)
2.7	2.682	2.664	2.646	2.628	2.61
2.85	2.832	2.814	2.796	2.778	2.76
3.0	2.982	2.964	2.946	2.928	2.91

Table 2  
Two possible end-member models for the Mojave crust

Crustal layers	Normal model		Mojave	Mojave-1 (no basalts)		Mojave-2	
	Velocity	Density		Temperature	Density	Temperature	Density
Upper	6.0	2.65–2.70	6.0	200	2.65–2.70	200	2.65–2.70
Middle	6.5	2.7–2.85	6.35	500	2.7–2.82	700	2.7–2.82
Lower	6.9	2.85–3.05	6.3	700	2.7–2.75	900	2.9–2.92

Table 3

Compilation of density limits  $\rho_i^{\text{up}}$  and  $\rho_i^{\text{low}}$  (see Eq. (A.3) in the Appendix A) and seismic P-wave velocities  $V_i$  (see Eq. (A.5) in the Appendix A) used in the gravity inversion

Density block $I$	$\rho_i^{\text{low}}$ (g/cm <sup>3</sup> )	$\rho_i^{\text{up}}$ (g/cm <sup>3</sup> )	$V_i$ (km/s)	Explanation
1	1.03	1.03		Water
<b>LARSE-1</b>				
Sediments				
2	1.70	1.80		“Normal” oceanic column, low density sediments (Layer 1A)
3	2.10	2.40		“Normal” oceanic column, high density sediments (Layer 1B)
4	1.70	1.90		Patton escarpment (shelf slope), Pliocene and younger sediments
5, 6	2.00	2.05		Nicolas forearc belt, Pliocene and younger sediments
7–12	2.50	2.60		Nicolas forearc belt, Cretaceous to Oligocene sediments
13–17	2.50	2.60		Nicolas forearc belt, Miocene sediments with volcanic intrusions
18	1.80	2.00		Nicolas forearc belt, Pliocene and younger
19, 20	2.50	2.60		Nicolas forearc belt, Cretaceous to Oligocene sediments
21–23	2.50	2.60		Nicolas forearc belt, Miocene sediments with volcanic intrusions
24–26	2.00	2.35		Catalina Schist belt, Pliocene and younger sediments
27–29	1.80	2.00		Catalina Schist belt, Quarternary sediments
30	2.00	2.10		Los Angeles basin, Quarternary sediments
31	2.00	2.30		San-Gabriel basin, Quarternary sediments
32–36	2.40	2.50		Los Angeles and San Gabriel basin, Pliocene sediments
37–42	2.50	2.60		Los Angeles and San Gabriel basin, Repeto formation sediments
43–47	2.60	2.70		Los Angeles and San Gabriel basin, lower sediments
48–51	2.45	2.55		Mojave Desert, Tertiary volcano-sedimentary basins
<b>Crust</b>				
52, 53	2.50	2.60		Franciscan basement, upper formation
54, 55, 56	2.60	2.70		Franciscan basement, lower formation
57, 58	2.50	2.60		Peninsula Ranges, overthrust Franciscan basement
59–66	2.70	2.75	5.57–5.64	Catalina schists, upper formation
67–75	2.80	2.90	6.17–6.25	Catalina schists, lower formation
76	2.70	3.00	6.29	Los Angeles basin, middle crust
77, 78	2.65	2.70	6.11, 6.31	San Gabriel basin, granitic basement
79	2.80	3.00	6.8	High-velocity body beneath San Gabriel basin
80, 81	2.70	2.80	6.12, 6.2	San Gabriel Mnts., Milonites
82, 83	2.72	2.75	6.0, 5.9	San Gabriel Mountains, Pelona schists, upper formation
84, 85	2.75	2.85	5.99, 6.01	San Gabriel Mountains., Pelona schists, lower formation
86, 87, 88	2.65	2.70	5.51–5.52	San Andreas fault, upper formation
89	2.70	2.75	5.8	San Andreas fault, lower formation
90, 91, 92	2.65	2.67	5.89–5.91	Mojave Desert, upper crust (intrusives + gneisses)
93	2.75	2.85	6.35	Mojave Desert, middle crust (gneisses + intrusives)
94	2.90	3.15	>7.0 (?)	Los Angeles basin, lower crust
95, 96	2.90	3.00	6.69, 6.5	San Gabriel basin and Mountains, lower crust
97	2.75	2.90	6.3	Mojave Desert, lower crust (gneisses or gabbros)
98	2.65	2.70		“Normal” continental column, upper crust
99	2.70	2.85		“Normal” continental column, middle crust
100	2.80	3.05		“Normal” continental column, lower crust
101	2.76	2.76	5.7	“Normal” oceanic column, basaltic (Layer 2)
102	2.78	2.78		Oceanic crust, basaltic (Layer 2)
103	2.95	2.95	6.65	“Normal” oceanic column, gabbroic (Layer 3)
104	2.96	2.96	6.7	Patton escarpment, gabbroic lower crust
105	2.97	2.97	6.75	Patton accretionary belt, gabbroic lower crust
106	2.98	2.98	6.8	Nicolas forearc and Catalina Schist belt, gabbroic lower crust
<b>Mantle</b>				
107	3.30	3.30	8.0	“Normal” oceanic lithospheric mantle
108, 109	3.15	3.45	8.0	Oceanic lithospheric mantle
110	3.10	3.45	7.98	

Table 3 (Continued)

Density block <i>I</i>	$\rho_i^{\text{low}}$ (g/cm <sup>3</sup> )	$\rho_i^{\text{up}}$ (g/cm <sup>3</sup> )	$V_i$ (km/s)	Explanation
111	3.10	3.45	7.95	
112, 119, 123	3.10	3.45	7.92	
113	3.10	3.45	7.89	
114	3.10	3.45	7.86	
115	3.10	3.45	7.83	
116	3.10	3.40	7.80	
117	3.05	3.40	7.68	Upper mantle beneath Catalina Schists belt
118	3.05	3.40	7.76	Upper mantle beneath Catalina Schists belt
120, 124, 133	3.10	3.45	7.84	
121	3.15	3.50	8.12	High-velocity body
122, 137	3.15	3.45	8.00	
125–128	3.10	3.45	7.92	
129–131	3.15	3.45	8.00	
132	3.05	3.40	7.76	Upper mantle beneath Mojave Desert
134	3.10	3.40	7.80	
135	3.10	3.40	7.80	“Normal” continental lithospheric mantle
136	3.10	3.45	7.90	“Normal” oceanic asthenosphere
138, 139	3.15	3.50	8.10	High-velocity body
140, 141	3.20	3.50	8.28	High-velocity body
142	3.20	3.50	8.22	High-velocity body
143–144	3.15	3.50	8.10	High-velocity body
145	3.15	3.50	8.10	“Normal” continental asthenosphere
LARSE-2				
Sediments				
146	1.03	1.03		Water
147	1.70	1.80		“Normal” oceanic column, low density sediments (Layer 1A)
148	2.10	2.40		“Normal” oceanic column, high density sediments (Layer 1B)
149	1.70	1.90		Patton escarpment (shelf slope), Pliocene and younger sediments
150, 151	2.00	2.05		Nicolas forearc belt, Pliocene and younger sediments
152–156	2.50	2.60		Nicolas forearc belt, Cretaceous to Oligocene sediments
157–160	2.50	2.60		Nicolas forearc belt, Miocene sediments with volcanic intrusions
161–163	2.00	2.35		Nicolas forearc belt, Pliocene and younger
164–167	2.00	2.05		Catalina Schist belt, Quaternary sediments
168–171	2.50	2.60		Catalina Schist belt, Cretaceous to Oligocene sediments
172–175	2.40	2.50		San Pedro basin, unsubdivided sediments
176–178	2.00	2.10		San Fernando and Santa Clarita Valleys, Quaternary sediments
179, 180	2.40	2.50		San Fernando, sediments $V_p = (2.4–2.7)$ km/s
181–186	2.50	2.60		San Fernando, sediments $V_p = (3.6–4.8)$ km/s
187	2.30	2.35		Mojave Desert, sediments of Tertiary Antelope basin,
Crust				
188, 189	2.50	2.60		Franciscan basement, upper formation
190–192	2.60	2.70		Franciscan basement, lower formation
193, 194	2.60	2.70		Peninsula Ranges, overthrust Franciscan basement
195–205	2.70	2.75	5.57–5.64	Catalina schists, upper formation
206–217	2.80	2.90	6.17–6.25	Catalina schists, lower formation
218	2.70	2.80	6.29	Granites or metamorphic sediments, S Fernando basin
219–221	2.65	2.70	6.30	Granitic basement, San-Fernando-Soledad basins
222	2.70	2.75	6.4	Granites, Transverse, middle crust
223	2.72	2.75	5.9	Pelona schist, upper (LA1–70)
224	2.75	2.85	6.0	Pelona schist, lower (LA1–139)
225–227	2.65	2.70	5.50	San Andreas fault, upper formation
228–231	2.85	3.00	6.5–6.7	Transverse Ranges, lower crust
232	2.65	2.67	5.9	Mojave Desert, upper crust (intrusives + gneisses)

Table 3 (Continued)

Density block <i>I</i>	$\rho_i^{\text{low}}$ (g/cm <sup>3</sup> )	$\rho_i^{\text{up}}$ (g/cm <sup>3</sup> )	$V_i$ (km/s)	Explanation
233	2.75	2.85	6.35	Mojave Desert, middle crust (gneisses + intrusives)
234, 235	2.70	2.92	6.3	Mojave Desert, lower crust (gneisses or gabbros)
236	2.65	2.67	5.91	Supplementary block., upper crust
237	2.70	2.75	6.36	Supplementary block., middle crust
238	2.70	2.92	6.31	Supplementary block., lower crust
239	2.65	2.70		“Normal” continental column, upper crust
240	2.70	2.85		“Normal” continental column, middle crust
241	2.80	3.05		“Normal” continental column, lower crust
242	2.76	2.76	5.7	“Normal” oceanic column, basaltic (Layer 2)
243	2.78	2.78		Oceanic crust, basaltic
244	2.95	2.95	6.65	“Normal” oceanic column, gabbroic (Layer 3)
245	2.96	2.96	6.7	Patton escarpment, gabbroic lower crust
246	2.97	2.97	6.75	Patton accretionary belt, gabbroic lower crust
247	2.98	2.98	6.8	Nicolas forearc and Catalina Schist belt, gabbroic lower crust
<b>Mantle</b>				
248	3.30	3.30	8.0	“Normal” oceanic lithospheric mantle, fixed density
249, 281	3.15	3.45	8.0	Oceanic lithospheric mantle
250	3.10	3.45	7.98	
251	3.10	3.45	7.95	
252	3.10	3.45	7.92	
253	3.10	3.45	7.89	
254	3.10	3.45	7.86	
255	3.10	3.45	7.83	
256, 278	3.10	3.40	7.80	
257	3.05	3.40	7.68	Upper mantle beneath Catalina Schists belt
258	3.05	3.40	7.76	Upper mantle beneath Catalina Schists belt
259, 261, 269	3.10	3.45	7.84	High-velocity body
260	3.05	3.40	7.76	High-velocity body
262	3.10	3.5	8.08	High-velocity body
263, 266, 267	3.10	3.5	8.0	High-velocity body
264	3.10	3.45	7.92	High-velocity body
265	3.15	3.50	8.12	High-velocity body
268, 270, 271	3.05	3.40	7.76	Low velocity body beneath Mojave Desert
272	3.15	3.5	8.28	High-velocity body
273, 275	3.15	3.5	8.14	High-velocity body
274	3.15	3.5	8.22	High-velocity body
276	3.10	3.5	8.06	High-velocity body
277, 279	3.15	3.50	8.10	High-velocity body
280	3.10	3.45	7.9	
282, 283	3.15	3.50	8.10	High-velocity body

Number of density block *i* refers to the number of density block shown in the density models (Fig. 3(b–e)).

### 2.1. The Pacific abyssal plain and Patton escarpment

The crustal thickness of the Pacific abyssal plain west of southern California was first estimated from seismic refraction experiments by Raitt et al. (1969). The density and thickness of the oceanic sediments (Layer 1) are both derived from the Deep Sea Drilling Project, and Ocean Drilling Project, Leg 63 site 468 (Patton escarpment) and site 469 (ocean to the west of the Patton escarpment) (Yeats et al., 1981; Yeats and Haq, 1981; Vedder et al., 1981) (Fig. 1b). The average densities of the upper (Layer 1A) and lower (Layer 1B) sedimentary layers are 1.7–1.8 g/cm<sup>3</sup>, and 2.1–2.4 g/cm<sup>3</sup>, respectively. The middle (basaltic) and lower (gabbroic) crustal densities (Layer 2 and 3) have been assigned in accordance with Carlson and Raskin (1984).

## 2.2. The Patton accretionary and Nicolas forearc belts

The structure of the marine sedimentary basins of the Patton accretionary and Nicolas forearc belts are taken from Bohannon and Geist (1998). The Patton accretionary belt is composed mostly of greywacke and argillite that is unmetamorphosed, or of low metamorphic grade, and is similar to parts of the Franciscan Complex. Densities are 2.5–2.6 g/cm<sup>3</sup> and 2.6–2.7 g/cm<sup>3</sup> for the upper and lower formations, respectively (Constenius et al., 2000). The Nicolas forearc belt is composed of 7–8 km thick volcano-sedimentary strata, similar to the Great Valley sequence (California) with densities of 2.5–2.6 g/cm<sup>3</sup> (Godfrey et al., 1997; Godfrey and Klemperer, 1998). This sedimentary complex is most likely underlain by Franciscan rocks to the west, and Catalina blueschists to the east (Bohannon and Geist, 1998). Miller (2002) proposes that this sedimentary complex is underplated by a mafic/ultramafic complex (“K” in Fig. 2) analogous to the “Great Valley ophiolite”. It is generally believed that the Pre-Miocene sediments and basement rocks are intruded by Miocene basic rocks. The intrusions may increase the bulk density of the sediments and low-density basement rocks by as much as 0.1 g/cm<sup>3</sup> when compared to the rocks that have not been influenced by magmatism (Table 3). Estimations of Moho depth beneath the Cortes bank are ~22 km (Shor and Raitt, 1958).

## 2.3. The Catalina Schist belt

The crustal structure of the Catalina Schist belt along the LARSE-1 and LARSE-2 profiles has been summarized by ten Brink et al. (2000), Godfrey et al. (2002) (LARSE-1), Fisher et al. (2003), Bohannon et al. (2004), and Baher (2004). In all of these articles, a low-velocity upper crust (~6.0 km/s) is noted, implying that the entire upper crust consists of Catalina schist. Based on laboratory measurements, the density of the Catalina schist is ~2.70 g/cm<sup>3</sup> (Langenheim, personal communication, 2001). Detailed upper crustal sections are taken from ten Brink et al. (2000). The configuration of the top of the basement and of the faults near the coast were taken from Wright (1991). At the base of the crust, ten Brink et al. (2000) interpreted velocities of less than 6.6 km/s as a slab gap in the oceanic plate, while Godfrey et al. (2002) and Nazareth and Clayton (2003) show a high velocity layer (6.6–6.8 km/s) which corresponds to fossilized oceanic crust. The existence of a high velocity layer at the base of the crust is supported by seismic results at other locations beneath the coastal regions (see summary in Fuis, 1998; Brocher et al., 1999). Crustal tomographic results (Sung and Jackson, 1992; Hauksson and Haase, 1997; Hauksson, 2000), though poorly constrained offshore, support Moho depths from teleseismic receiver function studies, and confirm a local Moho depth of ~22 km beneath the San Clemente and San Nicolas islands, and a Moho depth of ~27 km beneath the coast (Zhu and Kanamori, 2000; Magistrale, 2002).

## 2.4. The Los Angeles, San Fernando and San Gabriel basins

Data from oil wells in the Los Angeles, San Fernando, and San Gabriel basins provide structural and density information on local sediments (Wright, 1991; Wright and Yeats, 1997; Brocher et al., 1998; Langenheim et al., 2000). Based on seismic and other data (Magistrale and Zhou, 1996; Lutter et al., 1999, 2004; Fuis et al., 2001, 2003, 2004; Langenheim et al., 2000, 2004; Yeats and Huftile, 1995), basin depths at the profile location are estimated to be 8–9 km for the Los Angeles basin, and 5 km for the San Fernando and San Gabriel basins.

The seismic refraction model along the LARSE-1 line (Fuis et al., 2001) shows increasing velocities between 15–27 km beneath the Los Angeles basin with velocities of 6.1–6.5 km/s in the middle crust, and ~6.7 km/s in the lower crust. Beneath the San Gabriel basin, a high velocity body of 6.8 km/s is documented at mid-crustal levels. Beneath the Los Angeles basin, a 3-D tomography model shows systematically higher velocities of  $V_p > 6.8$  km/s at 20–26 km depth (Kohler and Davis, 1997), and  $V_p > 7.0$  km/s starting at ~18 km depth (Hauksson, 2000), which implies a possibly ultramafic lower crust with a bulk density of up to 3.15 g/cm<sup>3</sup>. The seismic structure of the lower continental crust is not well constrained by refraction data for the LARSE-2 line (Fuis et al., 2003).

## 2.5. The Transverse Ranges and San Andreas fault

The seismic velocity structure of the Transverse Ranges (San Gabriel and Pelona Mountains) is summarized in Lutter et al. (1999, 2004) and in Fuis et al. (2001, 2003), while deep seismic reflection information is summarized by Ryberg and Fuis (1998). Laboratory measurements of rock samples, collected around the LARSE-1 line, are reported by McCaffree Pellerin and Christensen (1998). The rocks of the upper crust of the San Gabriel Mountains have been

subdivided into two packages separated by the Vincent thrust fault (Ehlig, 1981). The upper package has a bulk density of 2.7–2.8 g/cm<sup>3</sup>, and is highly varied, consisting in part of a suite of Precambrian gneisses, amphibolites, and anorthosites. This upper package has also been intruded by granitic rocks and granodiorite. The lower package consists of the Pelona schist outcropping in the Pelona Mountains (LARSE-2 line). Some boundaries inside the crust are interpreted to intra-crustal blind thrusts, based on aftershock locations (Fuis et al., 2001, 2003). For the LARSE-1 line, the block around the main trace of the San Andreas fault, from the Punch-bowl to the Llano fault, is characterized by lower seismic velocities (5.5 km/s) and densities (2.65–2.67 g/cm<sup>3</sup>) due to the presence of cataclasite (McCaffree Pellerin and Christensen, 1998; Fuis et al., 2001).

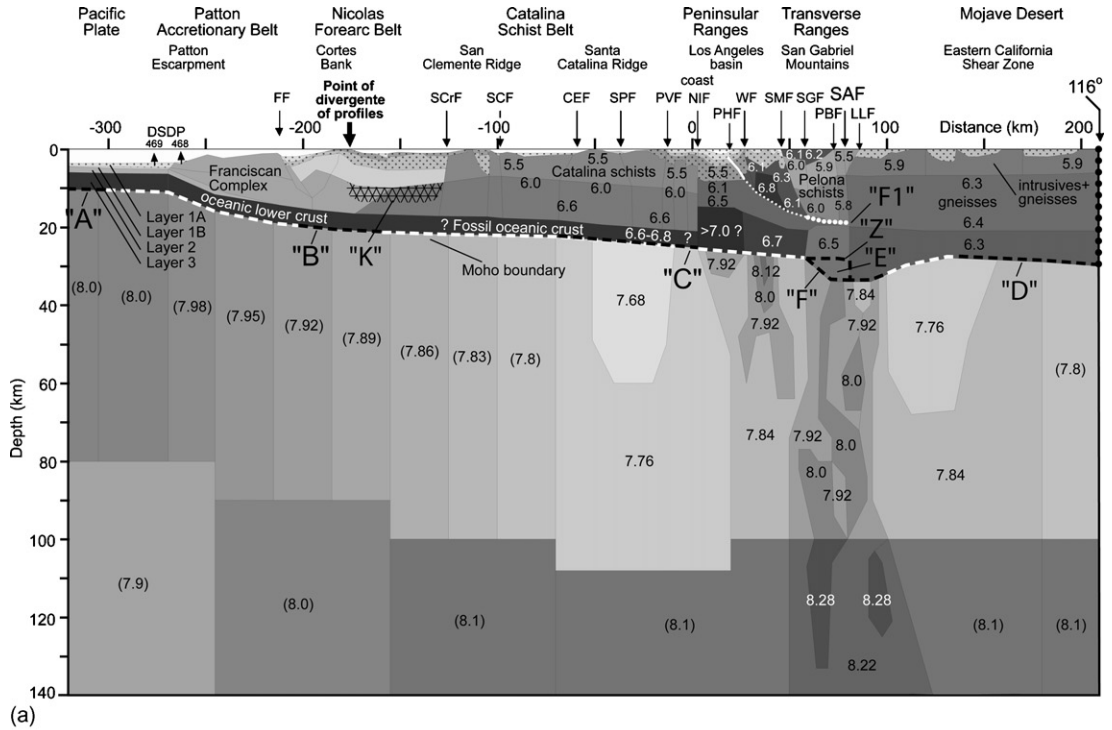
Detailed seismic investigations reveal a crustal root beneath the Santa Monica, San Gabriel, and San Bernardino Mountains (Sung and Jackson, 1992; Kohler and Davis, 1997; Richards-Dinger and Shearer, 1997; Zhu and Kanamori, 2000; Magistrale, 2002). The most reliable and detailed images of the Moho boundary beneath the San Gabriel Mountains and Mojave Desert along the LARSE-1 line (Zhu, 2000; Fuis et al., 2001) document not only a flat Moho throughout the entire Mojave province, at a depth of ~30 km, but also a modest crustal root of 3–5 km beneath the San Gabriel Mountains.

Below the San Andreas fault, Zhu (2000) shows a sharp drop in Moho depth of ~28 km beneath the San Gabriel Mountains (“Z” in Fig. 2), whereas Fuis et al. (2001) show a gently sloping Moho (“F1, F2” in Fig. 2). We prefer the F-Moho model because the direct ray-trace modeling of Godfrey et al. (2002) and Baher (2004) obtained seismic velocities in the lens between the “Z” and “F” Moho (“E” in Fig. 2) of 6.0–6.5 km/s. Thus, a crustal root may be centered beneath the San Andreas fault, at the LARSE-1 line, and is shifted westward relative the San Andreas fault at the LARSE-2 line. This represents a significant structural difference between the two lines.

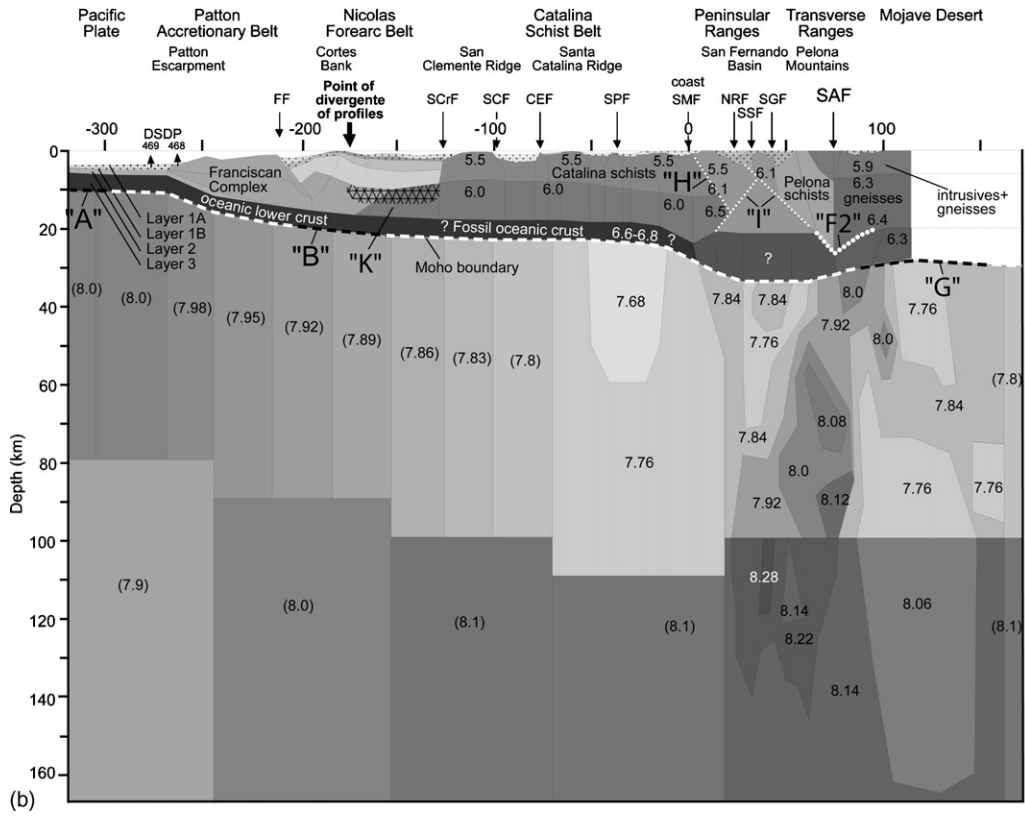
## 2.6. The Mojave province

The present-day relief of the central Mojave province consists of hills and elongated tectonic depressions (with depths >2–3 km from seismic and local geological estimates) that are filled with Tertiary volcanic and sedimentary rocks (Dokka, 1989; Glazner et al., 2000). Based on density modeling, Li et al. (1992a) estimate the density of the Tertiary sediments of the Antelope Valley (western Mojave, LARSE-2 profile) to be ~2.23 g/cm<sup>3</sup>. If the bulk composition of the synextensional sedimentary basins in the central Mojave province (LARSE-1 profile) intruded by Miocene plutons and dikes (Walker et al., 1995) is assumed to be 50% sediments (2.2–2.4 g/cm<sup>3</sup>), 25% granites (2.65 g/cm<sup>3</sup>), and 25% basalts (2.8 g/cm<sup>3</sup>), then the average density is 2.45–2.55 g/cm<sup>3</sup>.

The seismic structure of the Mojave province has been taken from Fuis et al. (2001) and Fuis et al. (2003) for the LARSE-1 and LARSE-2 lines, respectively. The imbricate character of the central Mojave province represents the alternation of elongated half grabens composed of normal fault-bounded blocks that lie above a rooted, low-angle detachment fault (Dokka, 1989). The detachment corresponds approximately to the top of a zone of increasing seismic velocities (from 5.9 to 6.3 km/s). Based on results of the Cajon Pass deep drillhole, Silver and James (1988) proposed that the Mojave crust contains gneissic lithology. Subsequently, Lutter et al. (1999) confirmed this by comparing velocity–depth curves obtained in laboratory rock samples, (McCaffree Pellerin and Christensen, 1998) with velocity–depth curves, obtained from seismic experiments. At a depth of 3–10 km, the bulk composition of the upper Mojave crust is mostly dominated by gneisses. However in the upper 3 km Lutter et al. (1999) conceded the possible existence of large intrusive bodies, which have been locally mapped in outcrops (Walker, 1995; Kenney and Weldon, 1998). We model the uppermost Mojave crust with velocities ~5.9 km/s as being composed of 50% intrusive and 50% gneissic rocks, with densities of 2.65–2.67 g/cm<sup>3</sup>. If the middle Mojave crust (seismic layer with velocities 6.3–6.4 km/s) is mostly gneissic, then densities of 2.8 g/cm<sup>3</sup> can be expected, according to the above estimates of McCaffree Pellerin and Christensen (1998), and possibly even 2.86 g/cm<sup>3</sup>, as reported by Malin et al. (1995). Alternatively, for a 50:50 granitic–gneissic composition, the density may be less than 2.75 g/cm<sup>3</sup>. For the Mojave lower crustal densities with an unusually low seismic velocity of ~6.3 km/s, we consider two possible end-member models (Table 2). The first model (“Mojave-1” in Table 2) corresponds to a typical three-layered platform crust with a mostly basic (mafic) lower crust. Low seismic velocities of ~6.3 km/s require extremely high crustal temperatures of up to 900–1000 °C, which would reduce the seismic velocities of basic rocks from the usual values of 6.8–7.0 km/s down to the observed values of 6.3 km/s, and correspondingly reduce density from about 3.0 g/cm<sup>3</sup> to 2.9 g/cm<sup>3</sup> (see Table 1). The second model (“Mojave-2” in Table 2) suggests the absence of a basic lower crustal layer. In this case, the temperature at the Moho boundary cannot exceed the temperature of wet granite melting, ~700 °C, and densities as low as 2.7 g/cm<sup>3</sup> can be



(a)



(b)

expected, i.e.  $\sim 0.05 \text{ g/cm}^3$  lower than mid-crustal densities. This variant with no mafic rocks in the Mojave crust is not very probable because (1) the analysis of Quaternary basalts from two volcanic craters (Glazner et al., 1991) implies the existence of at least minor mafic rocks in the Mojave crust; (2) thermal IR multispectral scanning results yielded the following bulk composition of rocks in the eastern Mojave Province: granitoids  $\sim 50\%$ , gneisses  $\sim 30\%$ , quartzites  $\sim 10\%$ , and amphibolites  $\sim 10\%$  (Hook et al., 1994).

Thus, the density of  $(0.1 \times 2.9 + 0.9 \times 2.7) = 2.72 \text{ g/cm}^3$  was adopted as the lower possible value. An additional indirect argument for even higher densities in the Mojave lower crust than  $2.72 \text{ g/cm}^3$  is the following: The postseismic relaxation recorded during the first few months following the Landers earthquake (1992) requires the lithospheric mantle temperature under the Mojave Desert to be intermediate between the dry and wet solidus of basalt,  $\sim 1000\text{--}1100 \text{ }^\circ\text{C}$  (Politz et al., 2000). Such a high mantle temperature implies a lower crust with a temperature greater than  $700 \text{ }^\circ\text{C}$ , and therefore a more basic composition of the lower crust.

## 2.7. The uppermost mantle

Tomographic studies of the seismic structure of the uppermost mantle of southern California resolve a near-vertical block beneath the Transverse Ranges, down to 200 km depth, with higher velocities of 8.0–8.3 km/s (Humphreys et al., 1984; Humphreys and Clayton, 1990; Zhao et al., 1996; Kohler and Davis, 1997; Kohler, 1999). The inner structure of the high velocity body, as resolved by the detailed seismic tomography model of Kohler (1999), is taken as the basis of the density models. The low velocity body ( $\sim 7.7 \text{ km/s}$ ), beneath the marine San Pedro basin and the Santa Catalina ridge, is accounted for by Humphreys and Clayton (1990), and qualitatively confirmed by Zhao et al. (1996).

## 2.8. Previous density models for southern California

Some early gravity models for southern California were simplified due to limited seismic information. Based on geological data, McCulloh (1960) first estimated, by 2-D interpretation, the gravity effect of the Los Angeles basin. Later, using seismic refraction data, Keller and Prothero (1987) compiled 2-D gravity crustal models along two profiles: a Santa Barbara–Santa Cruz Island–San Nicolas Island profile and a Patton escarpment profile. Recent models are more detailed. Along a segment of the COCORP profile (Cheadle et al., 1986) in the western Mojave Desert, Li et al. (1992a) modeled the Tertiary sediments of the Antelope Valley basin. Huftile and Yeats (1995) used isostatic residual gravity fields (Jachens and Griscorn, 1985) to create very detailed 2-D gravity models for three profiles across the Ventura sedimentary basin down to a depth of 15 km. Whole crustal-uppermost mantle density models were constructed along three profiles crossing the outer Borderland (Miller, 2002), along the seismic CALCRUST profiles in the San Bernardino (Li et al., 1992b) and Tehachapi Mountains (Malin et al., 1995), and along the LARSE-1 profile (Kohler, 1999; Langenheim, 1999). Langenheim and Hauksson (2001) compared the gravity field derived from a 3-D velocity model for the uppermost 10 km of the crust (Hauksson, 2000) with the observed isostatic residual gravity field, and found an excellent correlation. Kohler (1999) estimated a direct gravity impression of the high velocity upper mantle body to be a maximum of 50 mGal. Langenheim (1999) presented a detailed 2-D density model along the LARSE-1 line

---

Fig. 2. Seismic-geological cross-sections along LARSE-1 (a) and LARSE-2 (b) profiles (location of the profiles see Fig. 1) across the Borderland, Peninsula Ranges, Transverse Ranges, and Mojave Desert summarizing geological and geophysical data used to constrain the density models. The coast line is at 0 km distance in both profiles. Fault abbreviations: PBF: Punch-Bowl fault, LLF: Llano fault, PHF: Puente Hills blind thrust, SMF: Santa Monica fault, NRF: Northridge fault, SSF: Santa Susana fault, SAF: San Andreas fault, for other abbreviations see Fig. 1(a). Numbers with and without parentheses indicate estimated and measured seismic velocities (km/s), respectively. Estimations of Moho depth are taken from Zhu and Kanamori (2000) and Magistrale (2002). The Moho boundary is shown by a thick, white dashed line, black lines indicate locations where the Moho has been confirmed by refraction or reflection seismic experiments: “A”: for the Pacific plate (Raitt et al., 1969), “B”: beneath the Cortes Bank (Shor and Raitt, 1958), “C”: beneath the Santa Catalina Ridge (Godfrey et al., 2002; Nazareth and Clayton, 2003), “Z”: beneath the Transverse Ranges, “D”: beneath the eastern Mojave Desert (Zhu, 2000), “G”: beneath the Mojave Desert (Cheadle et al., 1986), “E”: crustal root beneath the Transverse Ranges (Baher, 2004). The black dotted line indicates a petrological ( $\text{Sr}_1 = 0.706$ ) boundary marking the western edge (at  $\sim 116^\circ\text{W}$ ) of the cratonic North American continental enriched mantle (Miller et al., 2000). The white dotted line within the crust for LARSE-1 line “F1” marks an intra-crustal blind thrust, as described by Fuis et al. (2001), for LARSE-2 line “F2” marks an intra-crustal structures, as described by Fuis et al. (2003). “H”: a proposed inclined boundary in the middle crust (Davis and Namson, 1994), “I”: a proposed inclined boundary in the middle crust (Tsutsumi and Yeats, 1999; Carena and Suppe, 2002). “K”: a proposed analogue of the Great Valley Ophiolite (Miller, 2002). DSDP 468 and 469 indicate the location of the Deep Sea Drilling Project, Leg 63 site 468 (Patton escarpment) and site 469 (ocean to the west of the Patton escarpment) (Yeats et al., 1981; Yeats and Haq, 1981; Vedder et al., 1981).

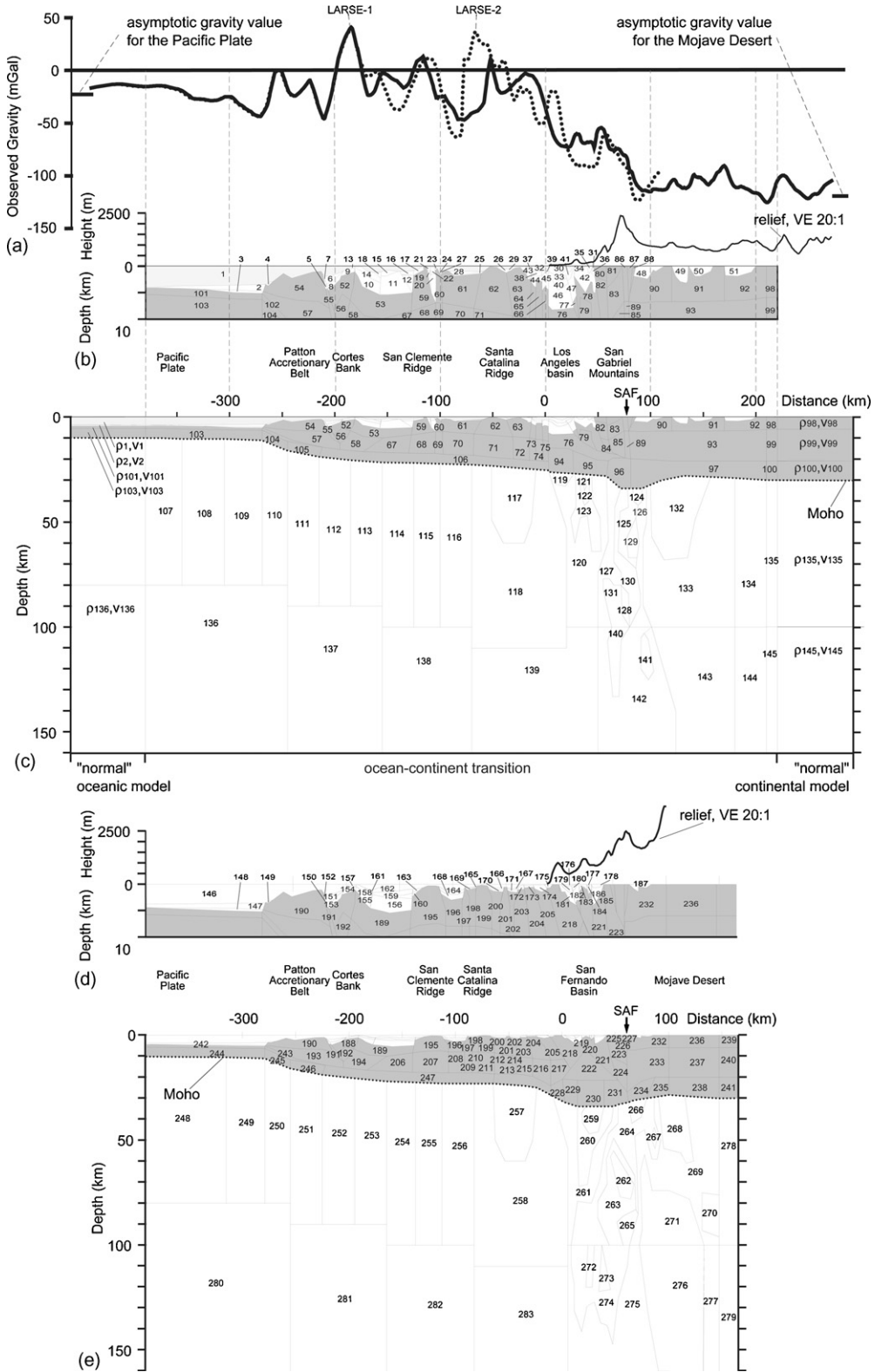


Table 4

Parameter setting  $C_p$ ,  $C_w$ ,  $b$  and  $\rho = a + bV$  used in the different modeling solutions R1–R15 (for the definition of the parameters see Eq. (A.4) in Appendix A), standard deviation of the gravity field  $\delta g$  (Eq. (A.1) in Appendix A) and isostatic pressure at the bottom of the model  $\delta p$  (Eq. (A.2) in Appendix A)

Solution	Density limits for the consolidated crust (g/cm <sup>3</sup> )	Density limits for the mantle (g/cm <sup>3</sup> )	$C_p$	$C_w$	$b$	$\rho = a + bV$	$\delta g$ (mGal)	$\delta p$ (bar)
R1	$\rho = 2.85$	$\rho = 3.3$	0	0			21.47	48.1
R2	See Table 3	$\rho = 3.3$	0	0			19.80	50.4
R3	See Table 3	See Table 3	0	0			5.73	265.9
R4	See Table 3	See Table 3	$10^3$	0			5.74	200.6
R5	See Table 3	See Table 3	$10^6$	0			5.78	20.4
R6	See Table 3	See Table 3	$10^7$	0			5.82	20.1
R7	See Table 3	See Table 3	$10^6$	$10^7$	$0 < b < 0.8$	$0.044 + 0.409 V$	5.97	20.0
R8	See Table 3	See Table 3	$10^6$	$10^9$	$0 < b < 0.8$	$0.174 + 0.390 V$	8.31	26.2
R9	See Table 3	See Table 3	$10^6$	$10^{11}$	$0 < b < 0.8$	$0.151 + 0.393 V$	11.73	26.3
R10	See Table 3	See Table 3	$10^6$	$10^9$	$b = 0$	3.3034	7.91	31.1
R11	See Table 3	See Table 3	$10^6$	$10^9$	$b = 0.1$	$2.502 + 0.1 V$	7.84	28.0
R12	See Table 3	See Table 3	$10^6$	$10^9$	$b = 0.2$	$1.701 + 0.2 V$	7.90	25.3
R13	See Table 3	See Table 3	$10^6$	$10^9$	$b = 0.3$	$0.899 + 0.3 V$	8.05	25.4
R14	See Table 3	See Table 3	$10^6$	$10^9$	$b = 0.4$	$0.097 + 0.4 V$	8.31	26.1
R15	See Table 3	See Table 3	$10^6$	$10^9$	$b = 0.5$	$-0.704 + 0.5 V$	8.67	28.2
R16	See Table 3	See Table 3	$10^6$	$10^9$	$b = 0.6$	$-1.504 + 0.6 V$	9.17	31.4

in the region, and showed that it is possible to fit the observed gravity field by constructing a model that compensates for the positive gravity effect of the high-density mantle body with the negative effect of a crustal root.

### 3. Gravity inversion method

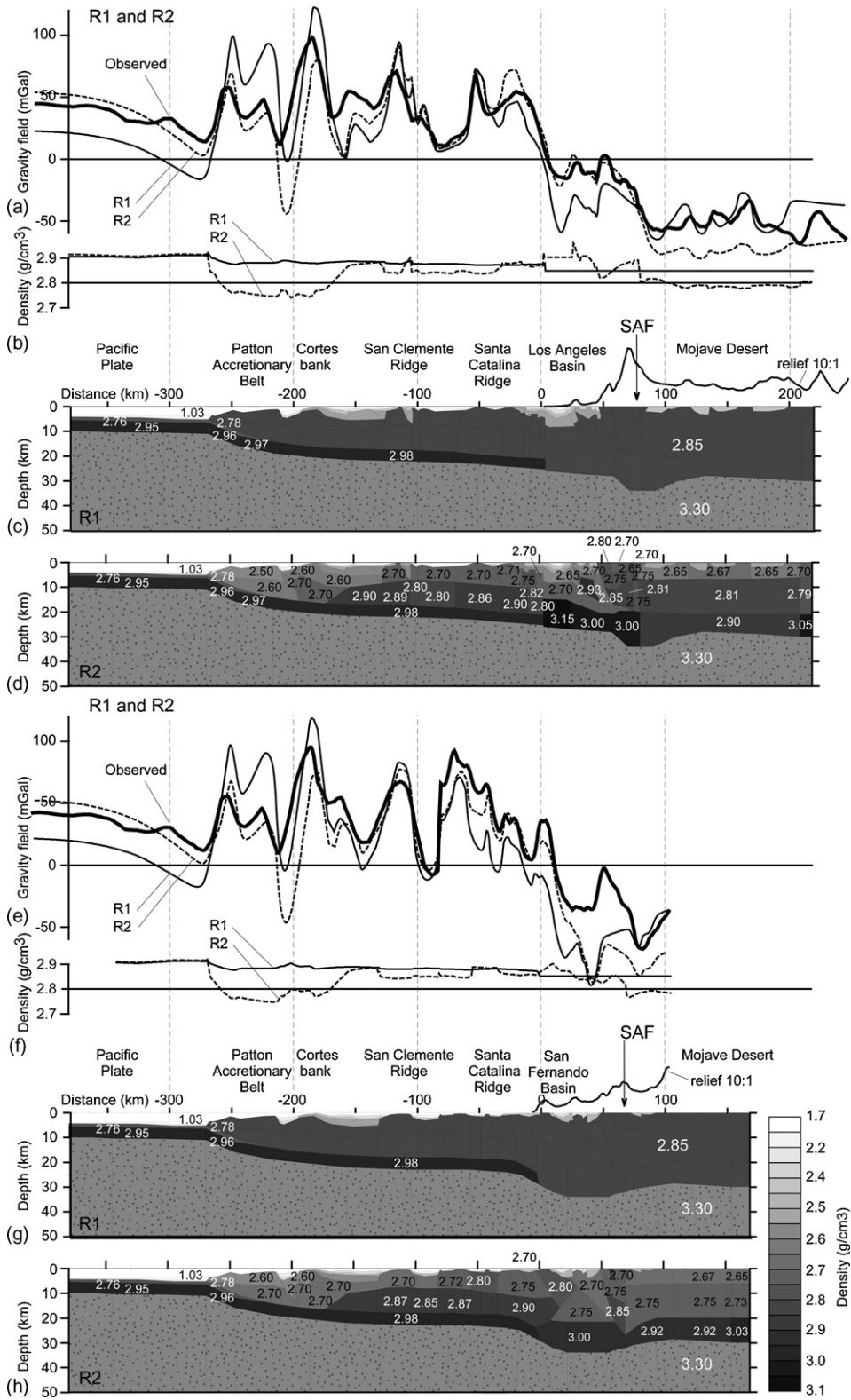
Our modeling approach is described in Appendix A. To constrain the model, we assume that the lithosphere is close to isostatic equilibrium at both ends of the profile, in the deep ocean and east of the Mojave Desert, and that densities ( $\rho$ ) show a linear correlation with seismic P-wave velocities ( $V_p$ ) in the mantle, i.e.  $\rho = a + bV_p$ . For all variables of the model, i.e. the densities of the blocks in the density cross section  $\rho_m$  (Fig. 3(b and c)), the constant  $G_0$  (Eq. (A.1) in the Appendix A), and parameters  $a$  and  $b$  in the linear velocity–density relation (Eq. (A.3) in the Appendix A), we use *a priori* constraints given by fixed lower (low) and upper (up) limits to exclude geophysically insignificant solutions.

#### 3.1. *A priori* constraints for the variables $\rho_m$ , $G_0$ , $a$ , and $b$ (Eq. (A.5) in the Appendix A)

Limits for the densities,  $\rho_m$ , of the model blocks are derived from the seismic-geological model (Fig. 2), and are summarized in Table 3, and Fig. 3. The densities of water (block 1), the “normal” oceanic middle and lower crust (blocks 100–103), the lower crust under the Borderland (block 104–106), and the “normal” oceanic lithospheric mantle (block 107) are kept constant because they bear the least uncertainties. The limits for  $G_0$  (Eq. (A.1) in the Appendix A) are allowed to vary widely because  $G_0$  is an artificial constant, which levels the gravity field, and whose value does not influence the final solution.

As previously mentioned, we assume a linear velocity–density relationship,  $\rho = a + bV_p$ , in the mantle where the estimation of the  $b$ -coefficient can be derived from laboratory measurements (Birch, 1961). Lateral variations of the upper mantle P-wave velocities are primarily due to changes in temperature, composition, anisotropy, partial melts,

Fig. 3. (a) Observed gravity curves along the profiles of Langenheim and Jachens (1996) and Wooley and Langenheim (2001) with asymptotic values over the Pacific plate of about  $-22$  mGal (free air anomaly) and over the Mojave Desert of about  $-120$  mGal (Bouguer anomaly). (b and d) Enlargement of the upper 10 km of the crustal structure (vertical exaggeration 5:1) and relief (vertical exaggeration 20:1) along the LARSE-1 (b) and LARSE-2 (d) profiles. Block numbers refer to densities and seismic P-wave velocities, which are listed in Table 3. (c and e) *A priori* density model (vertical exaggeration 2:1) of the upper 160 km; the lower mantle blocks expand vertically to the depth of 200 km, i.e. the base of the density model. Block numbers refer to densities and seismic P-wave velocities listed in Table 3. (SAF: San Andreas fault). On (c) a continuation of the ocean–continent transition by “normal oceanic” and “normal continental” models is shown beside the depth scale.



and fluid content. We can numerically estimate the influence of temperature and bulk composition on the general density–velocity relation, but we can only qualitatively argue why other factors can be neglected in the linear first order approach.

Variations in upper mantle composition are primarily due to varying degrees of basaltic melt removal. However, the influence of compositional changes on  $V_p$  is only minor, giving a  $b$  coefficient of  $\sim 0.09$  (g/cm<sup>3</sup>)/(km/s) (Jordan, 1978, 1981). Laboratory experiments on upper mantle rock samples reveal that near and far from the solidus temperature the  $b$ -coefficient is  $\sim 0.04$  (g/cm<sup>3</sup>)/(km/s) (Anderson and Bass, 1984; Duffy and Anderson, 1989), and  $\sim 0.18$  (g/cm<sup>3</sup>)/(km/s) (Sato et al., 1988, 1989; Sato and Sacks, 1989), respectively. Thus the combined effect of composition and temperature on the  $b$ -coefficient cannot exceed 0.27 (g/cm<sup>3</sup>)/(km/s). Birch's (1961) velocity–density bulk ratio coefficient of  $\sim 0.3$  (g/cm<sup>3</sup>)/(km/s), reflecting the influence of mineral composition without temperature–pressure effects, is higher than for a purely thermal effect. The basalt–eclogite transformation (gabbro:  $V_p = 7.0$  km/s,  $\rho = 3.0$  g/cm<sup>3</sup>; eclogite:  $V_p = 8.5$  km/s,  $\rho = 3.5$  g/cm<sup>3</sup>) would be the most important compositional change in downwelling lower crustal flow. A formal estimation of  $b = \Delta\rho/\Delta V_p$ , with  $\Delta\rho = 0.5$  g/cm<sup>3</sup> and  $\Delta V_p = 1.5$  km/s, gives an even higher  $b$ -coefficient of  $\sim 0.33$  (g/cm<sup>3</sup>)/(km/s). Superposition of all effects could result in a maximum  $b$ -coefficient of 0.6 (g/cm<sup>3</sup>)/(km/s). Therefore, the  $b$ -value is constrained to lie between 0 and 0.6 (g/cm<sup>3</sup>)/(km/s), whereas the  $a$ -value is allowed to vary widely. The standard error of velocity determination in the upper mantle  $\Delta V_j$  (Fig. 1A) is  $\sim 0.05$  km/s.

### 3.2. Isostatic analysis

A lack of correlation between Bouguer gravity and topography (Fig. 3) in southern California was recognized by McCulloch (1960). These observations, combined with the apparent lack of a significant crustal root beneath the San Gabriel and San Bernardino Mountains (Hadley and Kanamori, 1997) allowed Sheffels and McNutt (1986, 1987) to propose that the San Gabriel Mountains are not compensated by a classic “Airy root”, but are supported by elastic forces within the rigid lithosphere. Later, seismic data showed that there is in fact a 3–5 km deep crustal root, as well as a relatively high velocity body, beneath the San Gabriel Mountains, and present-day geodetic data show strong vertical and horizontal deformations. This implies more complicated regional tectonic behavior than simple static Airy isostasy, or the flexing of an elastic plate. At least a part of the regional topography should be supported dynamically, by flows in the mantle.

For these reasons, isostatic balance is only required at the “normal” continental and oceanic sections (Fig. 3(c)). To test the isostatic balance, weights of columns,  $p_n^{\text{mod}}$ , are calculated in 20 km wide strips at the left, and right ends of the cross-section (see Fig. A.1(b) in the Appendix A). In addition, we determine the deviation of the inner isostatic balance at each point of the density cross-section by calculating the difference between the lithostatic pressure of the model mass ( $\tilde{p}_i^{\text{mod}}$ ) and the mass of the “normal” oceanic column located over the point  $i$  ( $p_i^{\text{O}}$ ). The principle calculation of the deviation of the inner isostatic balance of the model is illustrated in Fig. A.1(b) (see Appendix A) and is given by:

$$\tilde{p}_i^{\text{mod}} = \tilde{p}_i^{\text{mod}} - p_i^{\text{O}} \quad (1)$$

$$\tilde{p}_i^{\text{mod}} = x_1 \rho_3 + x_2 \rho_{m+1} \quad (1a)$$

$$p_i^{\text{O}} = x_1^{\text{O}} \rho_1^{\text{O}} + x_2^{\text{O}} \rho_4^{\text{O}} + x_3^{\text{O}} \rho_6^{\text{O}}. \quad (1b)$$

Fig. 4. Modeling results of solution R1 and R2 for LARSE-1 and LARSE-2 profiles. Mantle densities are kept constant at 3.3 g/cm<sup>3</sup>, and no linear correlation of seismic P-wave velocities and densities ( $C_w = 0$ ), nor isostatic balance for the “normal” oceanic and continental columns ( $C_p = 0$ ) are required. In solution R2, a uniform crustal density 2.85 g/cm<sup>3</sup> is assumed except for oceanic crustal layers, water layer and sediments. In solution R2, crustal densities are allowed to vary within the limits shown in Table 3. (a and e) Comparison of modeled (R1 and R2) and the observed gravity curves along the LARSE-1 (a) and LARSE-2 (e) profiles (zero level of field corresponds to  $\sum g_k^{\text{obs}}/K$ ). (SAF—San Andreas fault). (b and f) Comparison of the vertically averaged density of the consolidated crust, i.e. crust without water and sediments, for solution R1 and R2 along the LARSE-1 (b) and LARSE-2 (f) profiles. (c and g) Density models for solution R1 (vertical exaggeration 2:1) and the relief (vertical exaggeration 10:1) along the LARSE-1 (a) and LARSE-2 (e) profiles. (d and h) Density models for solution R2 (vertical exaggeration 2:1) along the LARSE-1 (d) and LARSE-2 (h) profiles.

### 3.3. Estimations of the optimal and allowed discrepancies

In accordance with regularization theory, the optimal solution should have a discrepancy approximately equal to the standard deviation of the background noise.

The routine accuracy defining the deep seismic boundaries (e.g. the Moho boundary) along the profiles is estimated  $\sim 1$ – $2$  km. This results in corresponding errors in the modeled gravity field of about 12–15 mGal. Approximating the 3-D structure with a 2-D model leads to further errors. The offshore Borderland region is suitable for 2-D modeling because the profiles lie perpendicular to the structural grain. The Los Angeles basin, and especially the San Gabriel and San Fernando basins, are far less suitable for 2-D modeling because they have a more complex shape, and the profiles may cross them off-center. Additional error sources are given by structures and heterogeneities not found by seismic surveys and by the curvature of the profiles.

Each 100 m of topography adds  $\sim 30$  bars of lithostatic pressure. Modeled stress estimates in the lithosphere, stress drop estimates in earthquake sources, and empirical data on the ultimate strength of rocks suggest that a misfit of up to several kbars appears to be admissible for relative lithostatic pressure in cold lithospheric regions with viscosities of about  $10^{22}$ – $10^{24}$  P. However, the misfit should not be greater than 0.1–0.2 kbar at asthenospheric depth, nor in hot regions where viscosities are about  $10^{17}$ – $10^{18}$  P.

It is impossible to give an exact estimate of all potential errors, even those we know about. This implies that the gravity data can best be interpreted only in terms of regional trends and the larger anomalies.

## 4. Results and discussion

In the following section, we present several models, denoted as R1, R2, etc. The parameter settings of these models are compiled in Table 4. By changing the variables,  $\rho_m$ ,  $G_0$ ,  $a$ , and  $b$ , within the specified lower and upper limits, and the regularization parameters  $C_p$  and  $C_w$  (Eq. (A.4) in the Appendix A), it is possible to obtain a set of solutions. These solutions allow us to evaluate the ambiguity of the density models, and to find stable characteristics of the density distribution.

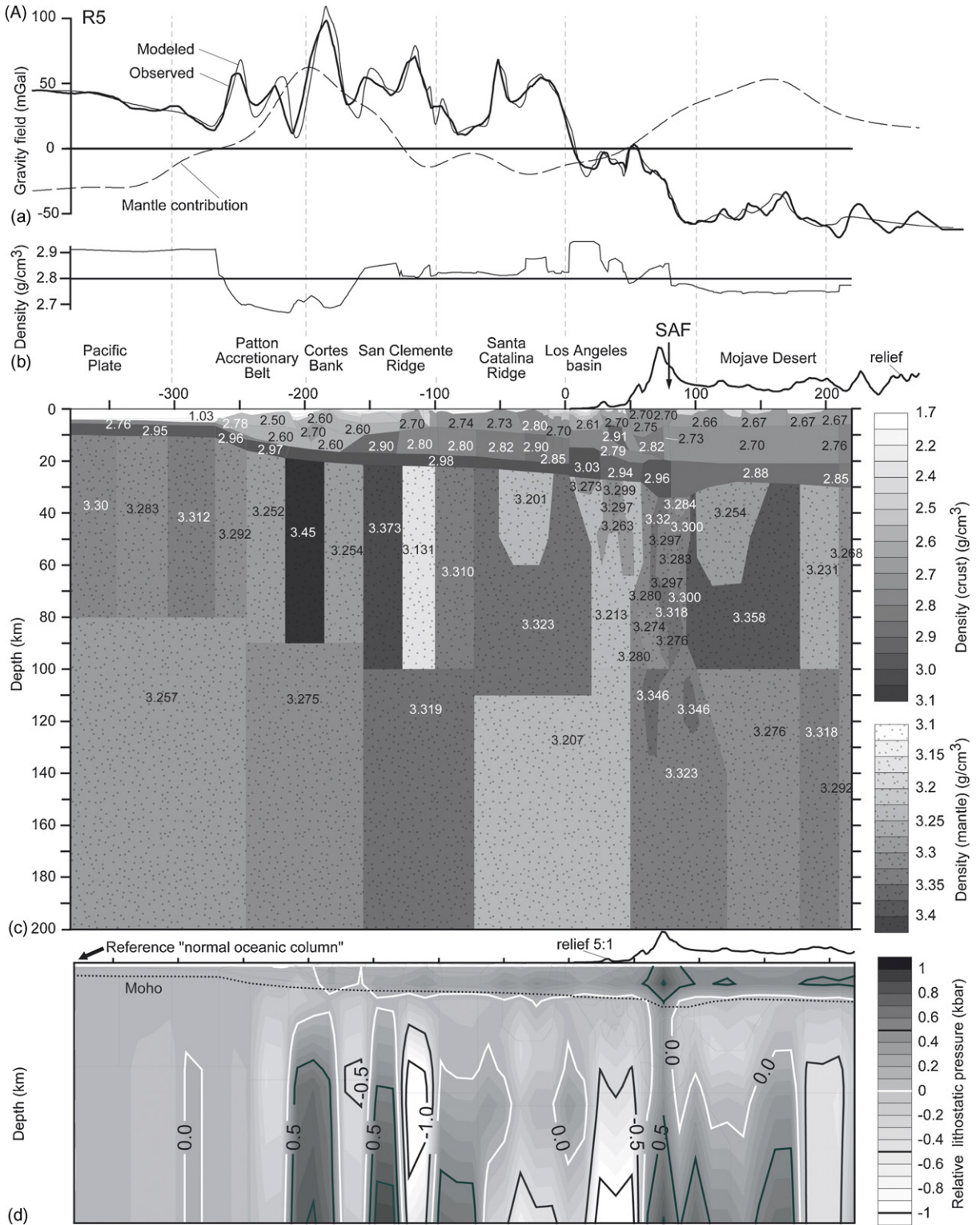
### 4.1. Solutions R1 and R2

Solutions R1 and R2 are obtained with requirements for neither isostatic balance nor for linear velocity–density correlation (i.e.  $C_p = C_w = 0$ ). By keeping mantle densities constant at  $3.3 \text{ g/cm}^3$ , and by successively refining the crustal density structure, the influence of the crustal density features can be isolated.

In solution R1 (Fig. 4), we can distinguish the water layer, the sedimentary basins, the layers of the “normal” oceanic crust, and the lower crust under the Borderland. Densities in these blocks are allowed to vary within the limits given in Table 3. The remaining blocks of the crust have been set to a constant density of  $2.85 \text{ g/cm}^3$ . As a result, this model shows roughly the gravity effects of the water layer, the sedimentary basins, and the undulations of the Moho boundary ( $\delta\rho = 0.45 \text{ g/cm}^3$ ). The shapes of the anomalies over the Borderland are mostly due to changes in water depth. Because the amplitudes of the modeled field are much larger than those observed, the average crustal density of the Borderland should be somewhat lower than  $2.85 \text{ g/cm}^3$ . The modeled small-scale gravity minima over the Los Angeles and San Gabriel basins in the LARSE-1 profile are greater than the observed minima. In the LARSE-2 profile, for a large segment of the profile from the Santa Catalina ridge to the San Andreas fault, the modeled gravity curve is lower than observed. Over the San Fernando basin, the difference reaches  $\sim 50$  mGal. For both profiles, the gravity asymptotic levels are not a good fit, which suggests average density variations are needed in either the crust or mantle.

---

Fig. 5. Modeling results of solution R5 along the LARSE-1 (A) and the LARSE-2 (B) profiles. Densities in both the crust and mantle are allowed to vary within the limits shown in Table 3. The isostatic balance for the “normal” oceanic and continental columns is taken into account ( $C_p = 10^6$ ), but no linear correlation of seismic P-wave velocities and densities is required ( $C_w = 0$ ). (a) Modeled and observed gravity curves along the profile (zero level of field corresponds to  $\sum g_k^{\text{obs}}/K$ ) and the gravity contribution of the mantle, which is estimated by assuming a constant density of  $3.3 \text{ g/cm}^3$  for the crust, with a water layer included. (b) Vertically averaged density of the consolidated crust, i.e. crust without water or sediments. (c) Density model (vertical exaggeration 2:1) and relief (vertical exaggeration 10:1) along the profile. (SAF–San Andreas fault) (d) Distribution of the modeled lithostatic pressure deviations relative to the “normal” oceanic column, showing the inner isostatic imbalance of the model. White lines are “levels” of isostatic compensation.



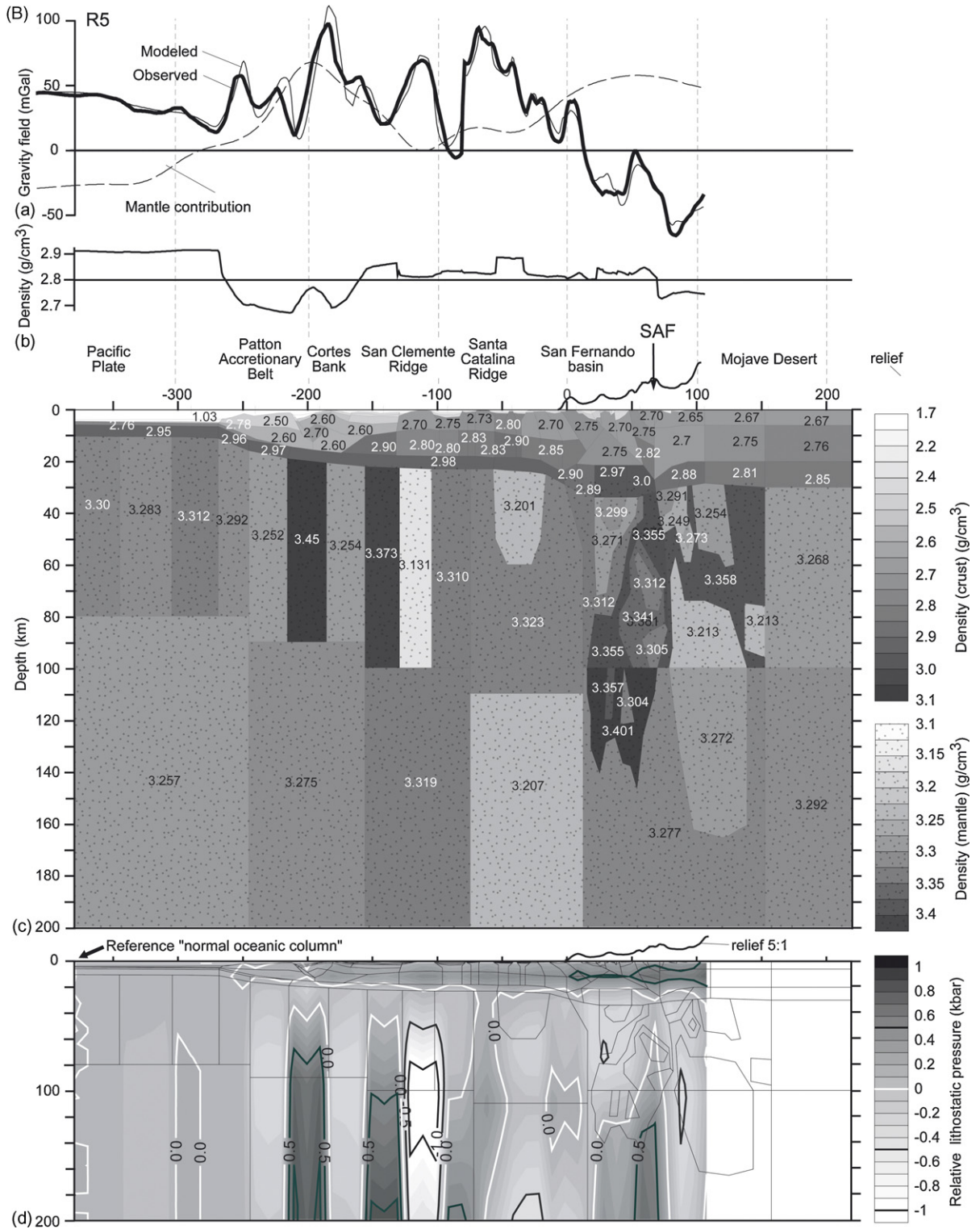


Fig. 5. (Continued).

In solution R2 (Fig. 4), all crustal densities are allowed to vary within the estimated limits (Table 3). By allowing density heterogeneities within the entire crust, the gravity fit is generally improved. However some areas in both profiles are still not reasonably fitted (the Cortes bank on both profiles, Mojave Desert on the LARSE-1 profile, and Santa Catalina Ridge and the whole continental segment on the LARSE-2 profile). To compensate for low gravity values beneath the Los Angeles basin, our R2 model suggests an unusually high density of  $3.15 \text{ g/cm}^3$  in the lower crust. In LARSE-2, the misfit between the observed and the modeled curves extends for a large segment of the profile.

There is no seismic data to fully constrain the Moho boundary depth in the transition zone from the Pacific Ocean to the Patton accretionary belt. Therefore, several models, wherein the oceanic Moho boundary slopes from 10 km in the deep ocean to as much as 13 km at the boundary to the Patton escarpment, are evaluated. The best agreement with the observed slope of the gravity curve is achieved with a very gently sloped Moho boundary which deepens to no more than 11 km at the boundary to the Patton escarpment. Our result agrees generally with that of Keller and Prothero (1987) who suggested a density model with low upper crustal densities ( $2.5\text{--}2.6 \text{ g/cm}^3$ ) in the Patton escarpment, and a Moho boundary that is horizontal under the ocean, but sharply deepens beneath the Patton escarpment.

We obtained a very high density  $2.9 \text{ g/cm}^3$  in the crustal block underlying the sedimentary complex of the San Nicolas Basin. Density is  $\sim 0.1 \text{ g/cm}^3$  higher than in the other blocks composed of the lower section of Catalina schist. Moreover, even the uppermost mantle block beneath this basin shows an unusually high density. This result indicates that: (1) only the small western part of the San Nicolas basin can be underlain by the low-density Franciscan complex, with most of the basin underlain by higher density rocks; (2) Miller (2002) executed gravity modeling along three profiles crossing the San Nicolas Basin (Fig. 1) and showed a block (“K” in Fig. 2) beneath the San Nicolas basin on all 3 profiles with unusually high density. Miller (2002) interpreted this block as a continuation or an analog of a Great Valley Ophiolite, and found the density to be  $3.0 \text{ g/cm}^3$ . Although Miller (2002) used higher densities for Franciscan rocks than is commonly adopted (she believed that they were intensively and widely intruded by Miocene volcanics), her estimation concerning this high density block agrees with our density definition. To show this, we subdivide block 67 with a density of  $2.9 \text{ g/cm}^3$  into two halves (each  $\sim 5 \text{ km}$  thick), and consider the upper half as a Great Valley Ophiolite with a density of  $3.0 \text{ g/cm}^3$  and the lower half as a continuation of the lower package of Catalina schist with a density of  $2.8 \text{ g/cm}^3$ .

#### 4.2. Solutions R3, R4, R5 and R6

In R3, R4, R5 and R6, the densities found both in the crust and mantle are allowed to vary within the limits shown in Table 4, and no linear correlation of seismic P-wave velocities and densities is required ( $C_w = 0$ ).

Solution R3 is obtained without requirements for isostatic balance ( $C_p = 0$ ). Although the gravity field fit is perfect, the density model results in an isostatic imbalance of 265 bar between the “normal” oceanic and continental columns at the bottom of the model ( $\delta p$  in Table 4). If all the density differences between columns were condensed in relief, this

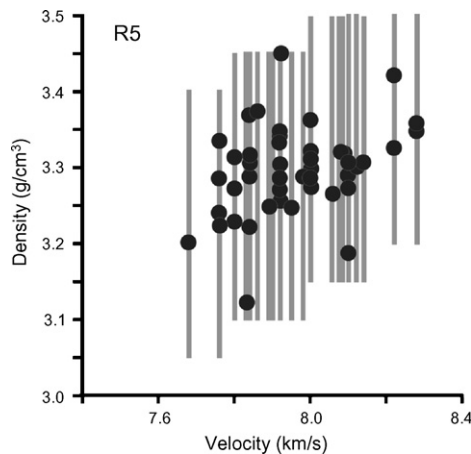


Fig. 6. Velocity–density diagram for solution R5. Each point in the diagram corresponds to a single mantle density block from the cross-sections shown in Fig. 5.

would amount to  $\sim 1$  km of uncompensated topography. By going from a simplified (R1) to a more complex (R3) density structure, the gravity fit improves ( $\delta g$  in Table 4), but results in an isostatic imbalance that is too large. By increasing the parameter  $C_p$  from 0 to  $10^6$  (R3, R4, R5 in Table 4), the isostatic balance of the “normal” oceanic and continental columns is improved to  $\delta g \approx 20$  bar ( $\sim 70$  m of uncompensated topography) without any significant influence on the

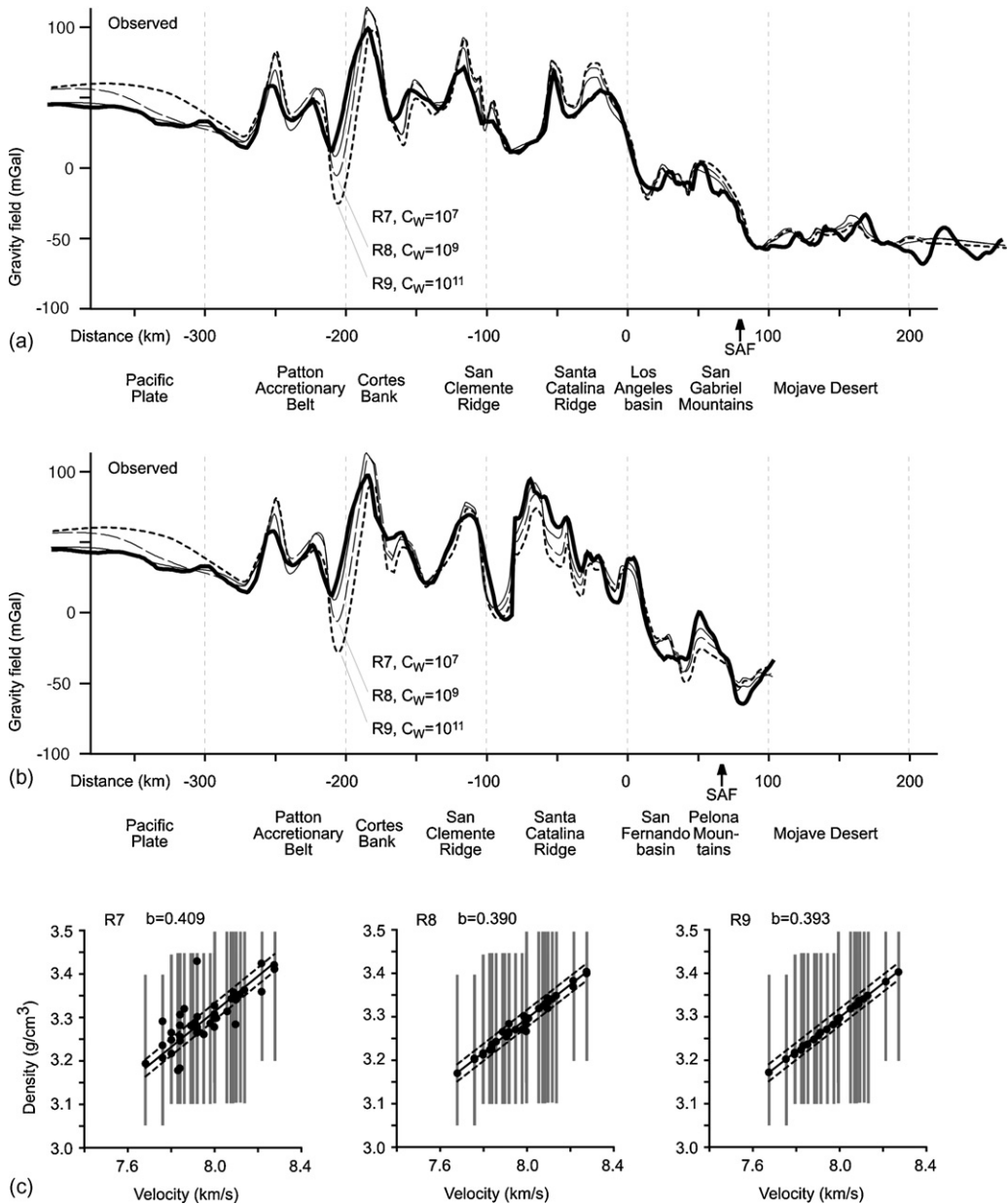


Fig. 7. Comparison of solutions R7, R8, and R9. Densities are allowed to vary within the limits shown in Table 3, isostatic balance for the “normal” oceanic and continental columns is required ( $C_p = 10^6$ ), and a linear correlation of seismic P-wave velocities and densities in the mantle is taken into account with different weighting factors, i.e. for R7– $C_w = 10^7$ , R8– $C_w = 10^9$ , R9– $C_w = 10^{11}$ . (a and b) Comparison of the modeled and observed gravity curves along the LARSE-1 (a) and LARSE-2 (b) profiles (zero level of field corresponds to  $\sum g_k^{obs}/K$ ) for solution R7, R8, and R9. (SAF–San Andreas fault). (c) Velocity–density diagrams for solutions R7, R8, and R9 where each point in the diagram corresponds to one mantle density block of the cross-sections. The linear approximation  $\rho = a + bV$ , as determined during inversion, is shown by a thick solid line, while the dashed lines mark the stripe (band) of  $\pm \Delta V = 0.05$  km/s which is the standard error of the velocity determination in the upper mantle. Gray bars correspond to allowed density range variations, i.e.  $\rho_m^{low} < \rho_m < \rho_m^{up}$  in relation (A.5) in the Appendix A (see also Table 3).

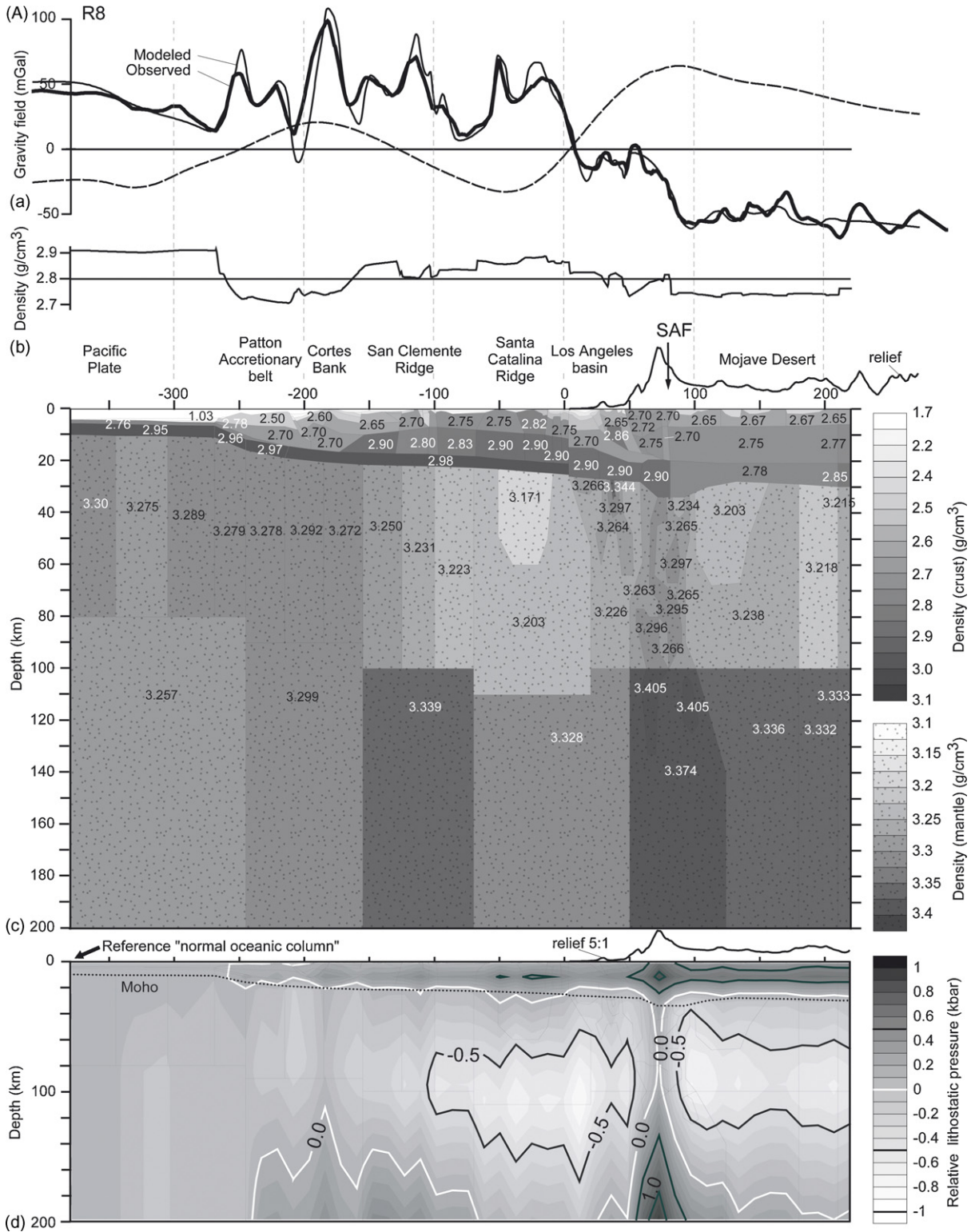


Fig. 8. Modeling results of solution R8 along the LARSE-1 (A) and LARSE-2 (B) profiles. Densities in both the crust and mantle are allowed to vary within the limits shown in Table 3, isostatic balance for the “normal” oceanic and continental columns is taken into account ( $C_p = 10^6$ ), and a linear correlation of seismic P-wave velocities and densities is required (i.e.  $C_w = 10^9$ ), whereas the  $b$ -coefficient is allowed to vary between 0 and 0.8. A best-fit value of  $b = 0.39$  was obtained. For further explanation see Fig. 5.

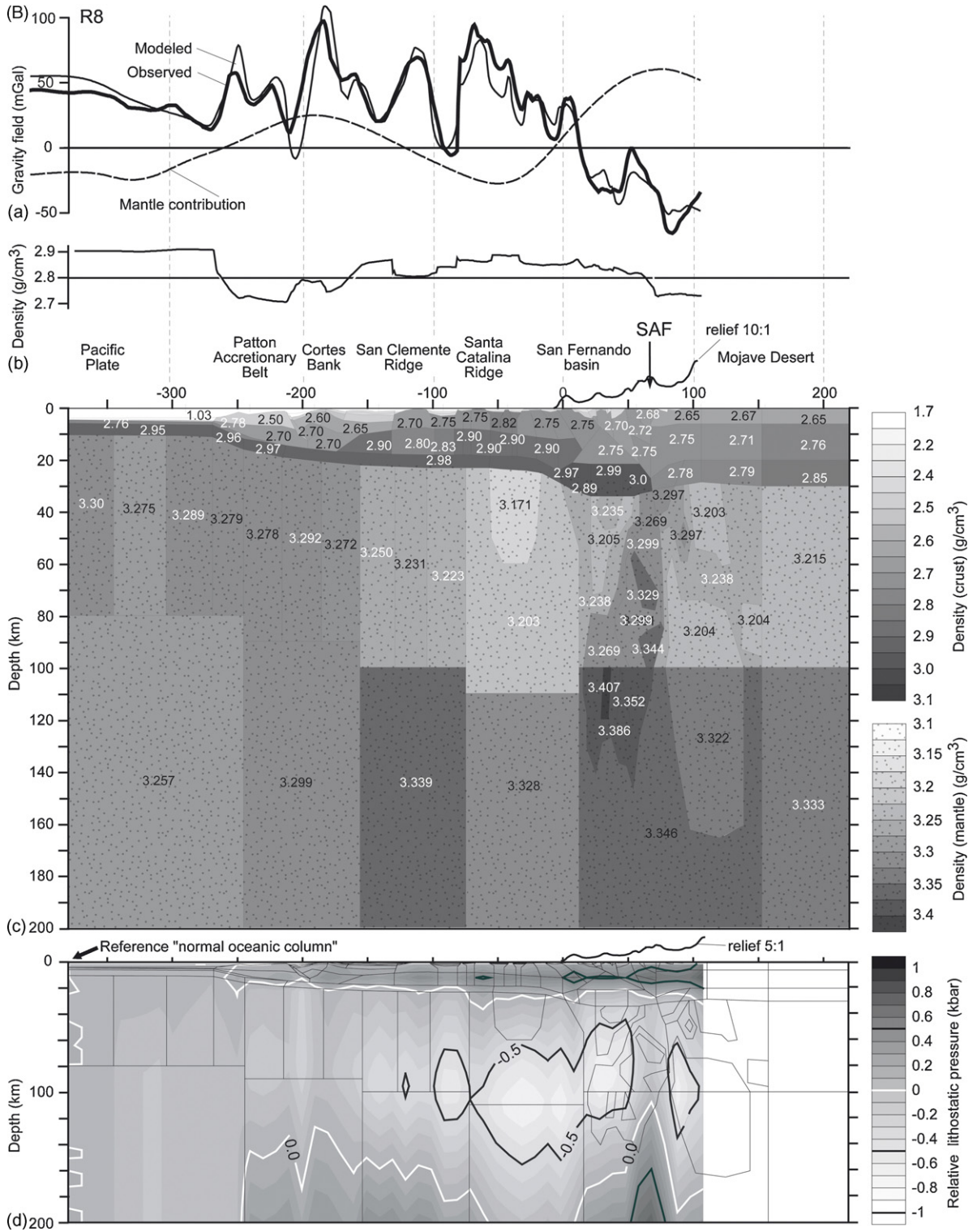


Fig. 8. (Continued).

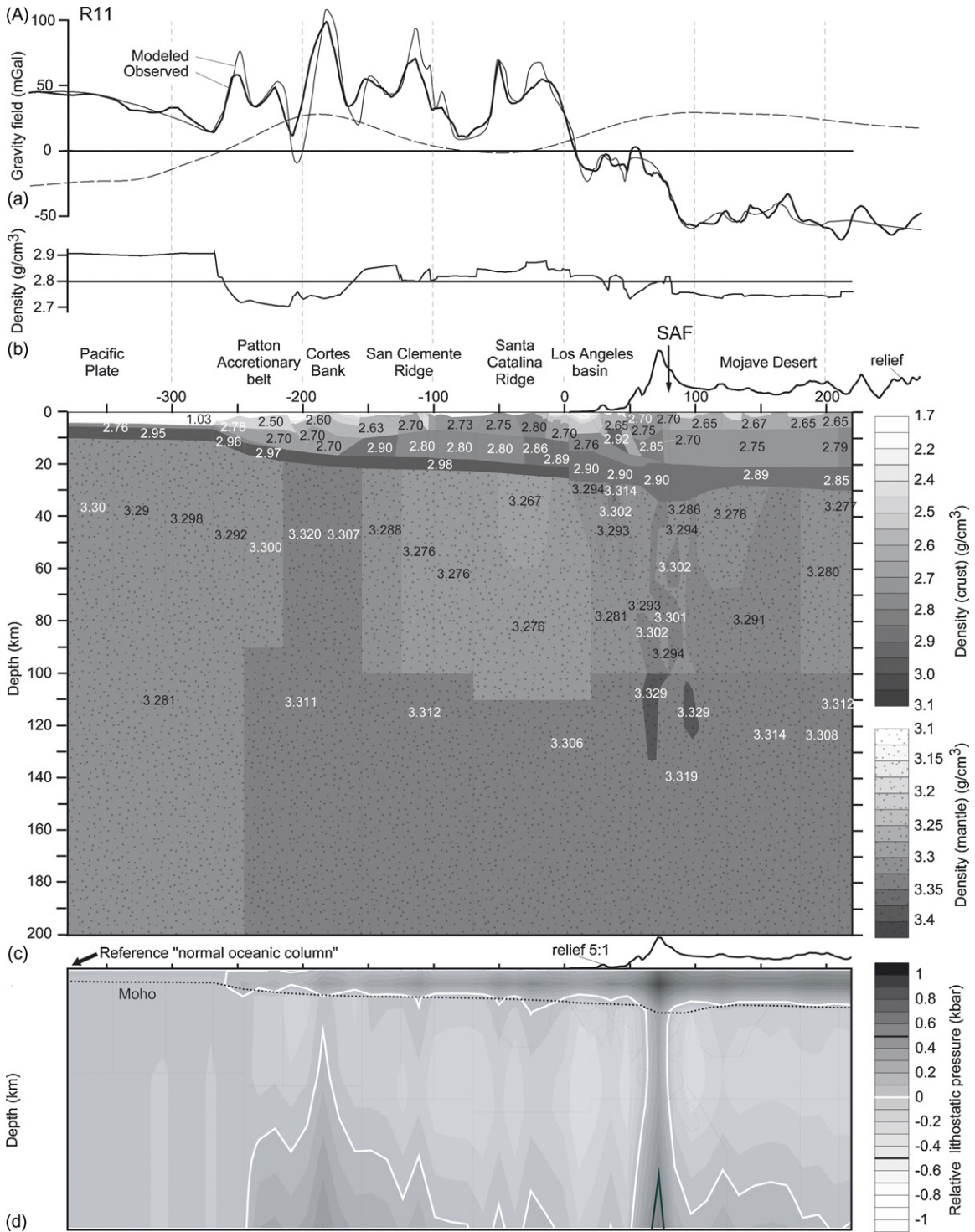


Fig. 9. Modeling results of solution R11 along the LARSE-1 (A) and LARSE-2 (B) profiles. Densities in both the crust and mantle are allowed to vary within the limits shown in Table 3, isostatic balance for the “normal” oceanic and continental columns is taken into account ( $C_p = 10^6$ ), and a linear correlation of seismic P-wave velocities and densities is required (i.e.  $C_w = 10^9$ ). The  $b$ -coefficient has been predefined to be  $b = 0.1$ . For further explanation see Fig. 5.

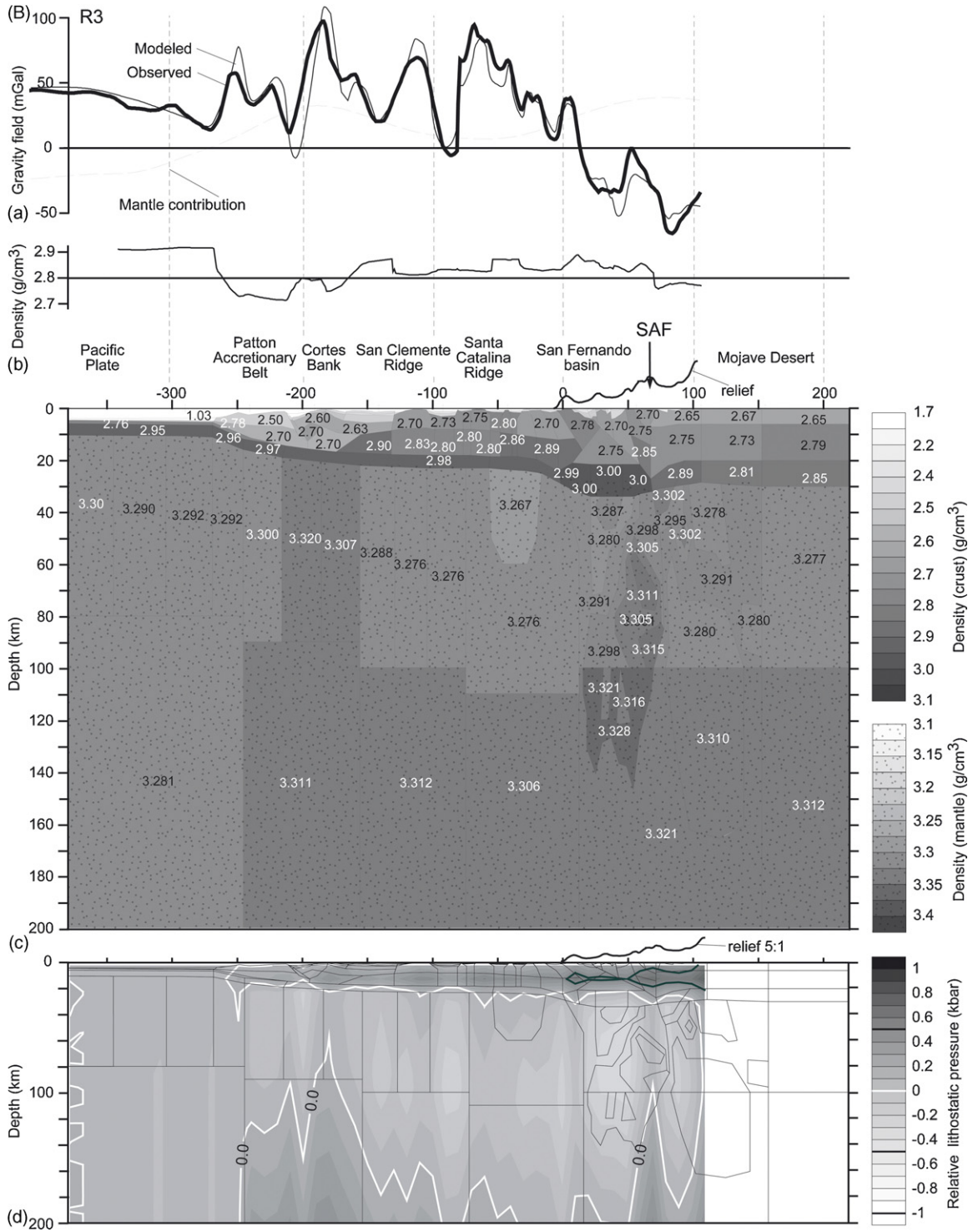


Fig. 9. (Continued).

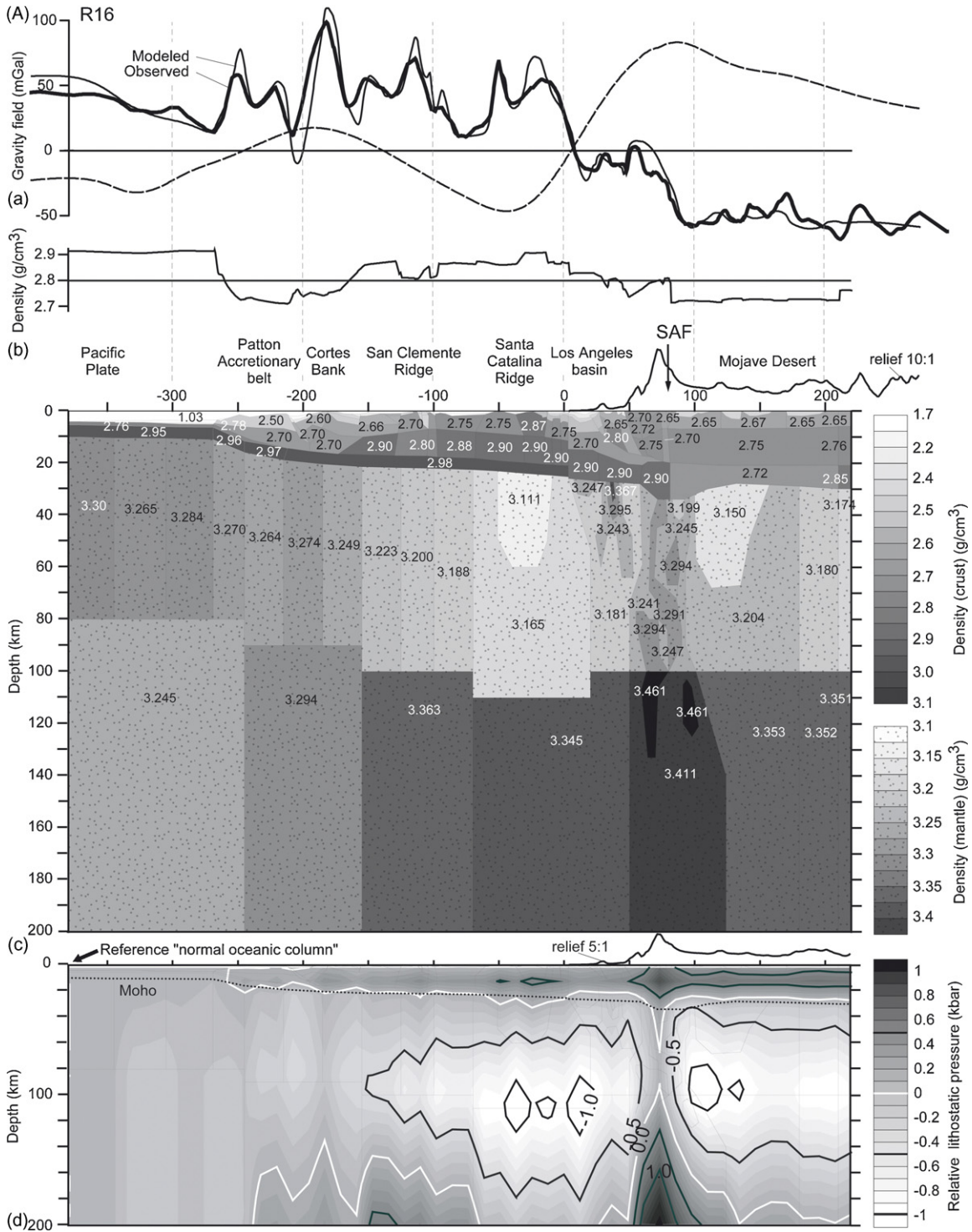


Fig. 10. Modeling results of solution R16 along the LARSE-1 (A) and LARSE-2 (B) profiles. Densities in both the crust, and mantle, are allowed to vary within the limits shown in Table 3. The isostatic balance for the “normal” oceanic and continental columns is taken into account ( $C_p = 10^6$ ), and a linear correlation of seismic P-wave velocities and densities is required (i.e.  $C_w = 10^9$ ). The  $b$ -coefficient has been predefined to be  $b = 0.6$ . For further explanation see Fig. 5.

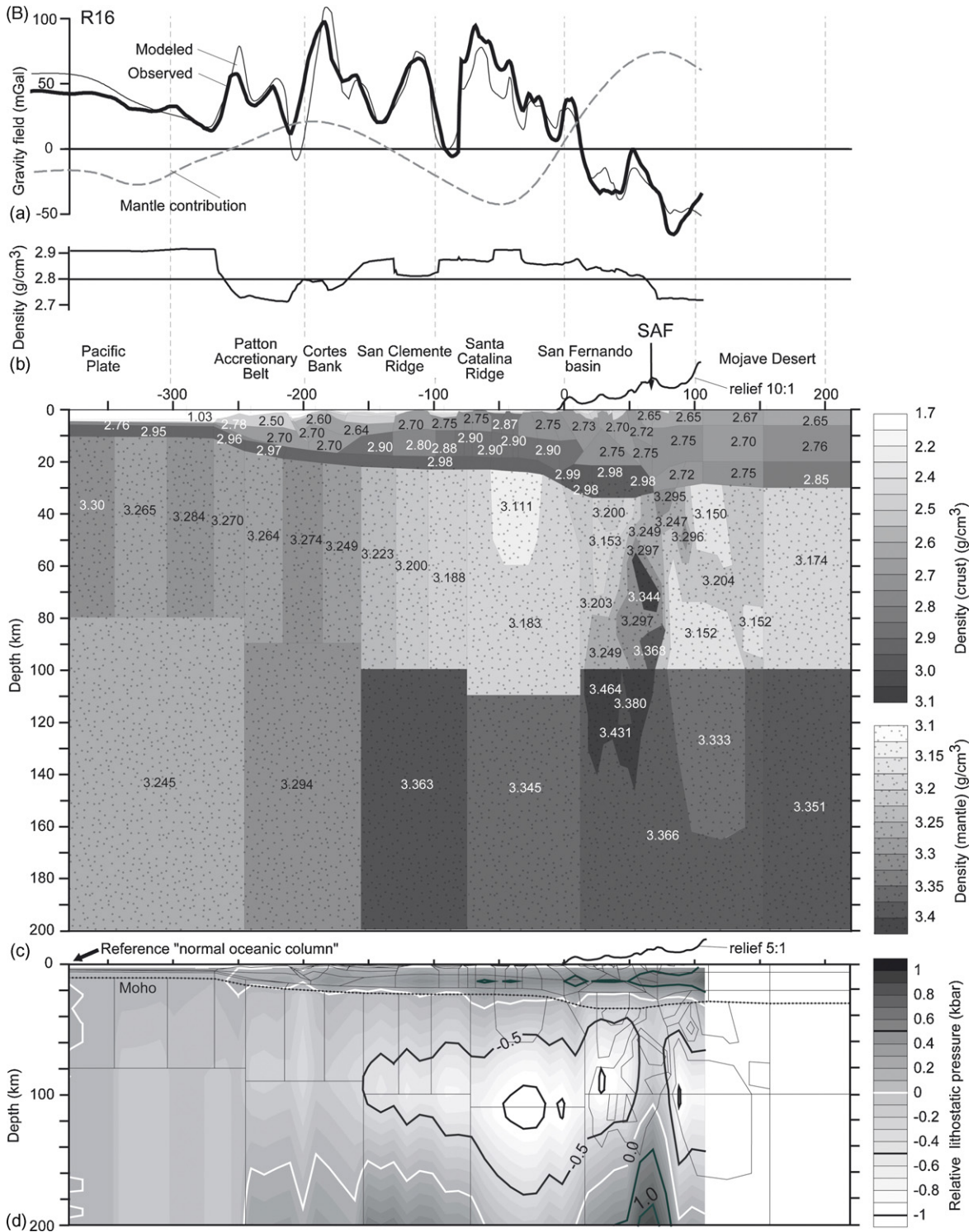


Fig. 10. (Continued).

gravity fit in the ocean–continent transition zone. Increasing the  $C_p$  parameter further does not influence the solution (R6 in Table 4).

Solution R5 (Fig. 5) produces strong variations in mantle densities. As is evident from the seismic–geological section (Fig. 2), the model shows increased densities under the Transverse Ranges, with adjacent areas of decreased densities. The short wavelength density heterogeneities under the Borderland are unreasonable. Furthermore, local isostatic imbalance in the inner part of the mantle reaches an unrealistic value of over 1 kbar, and mantle velocity–density points are scattered chaotically in the velocity–density diagram with no linear correlation (Fig. 6).

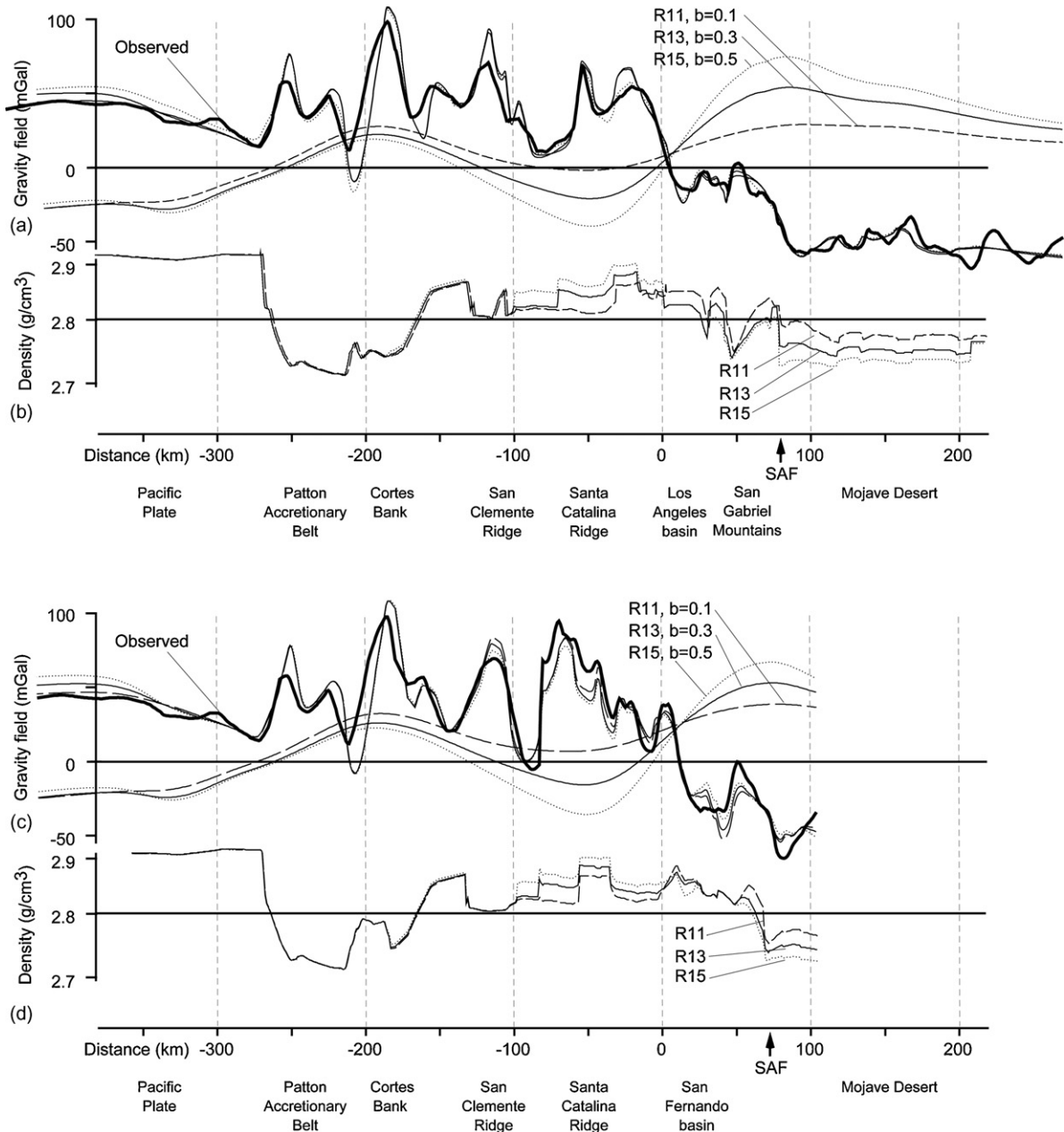
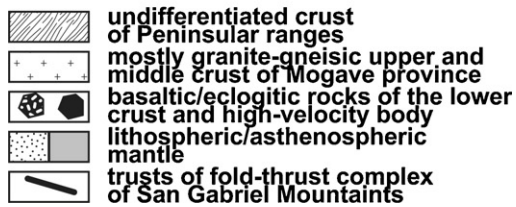
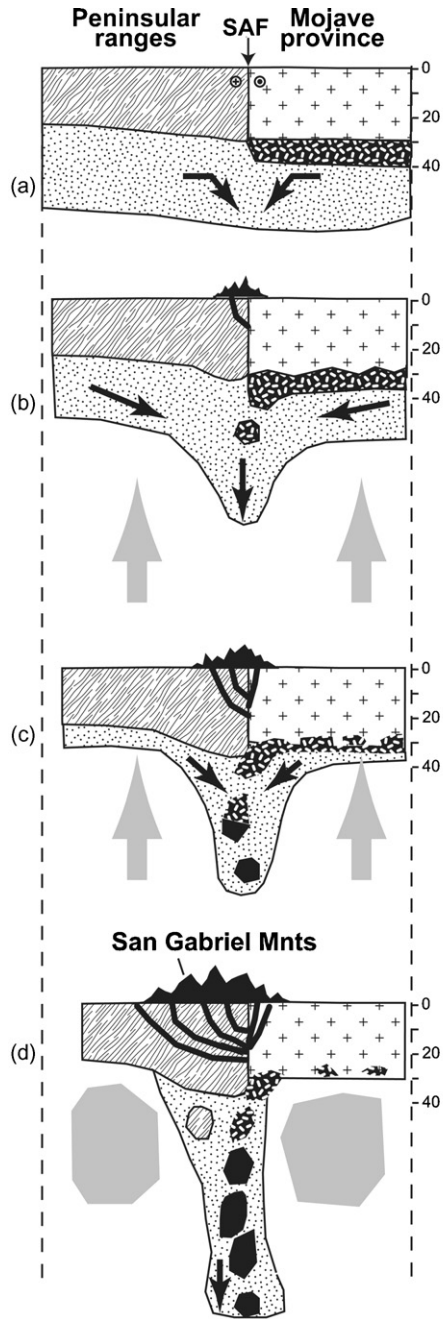


Fig. 11. Comparison of solution R11 ( $b=0.1$ ), R13 ( $b=0.3$ ) and R15 ( $b=0.5$ ). (a) Modeled and observed gravity curves along the profile (zero level of field corresponds to  $\sum g_k^{obs}/K$ ) for solutions R11, R13 and R15. The gravity contribution of the mantle, estimated by assuming a constant density of  $3.3 \text{ g/cm}^3$  for the crust with a water layer, is also included. (b) Vertically averaged density of the consolidated crust, i.e. crust without water or sediments, for solutions R11, R13 and R15. (SAF–San Andreas fault).



#### 4.3. Solutions R7, R8, and R9

In solutions R7, R8, and R9, all densities are allowed to vary within the estimated limits (Table 3) and  $C_p$  is set to  $10^6$ —i.e. parameter settings as in model R5. In addition, we require that densities in the mantle correlate with seismic P-wave velocities, i.e.  $C_w \neq 0$ . In Fig. 7, three examples of solutions (R7, R8, R9) with increasing  $C_w$ -values are shown. In the R7 solution at a low  $C_w$ -value, the velocity–density points are scattered more than we would expect with the routine accuracy of seismic velocities ( $\Delta V = 0.05$  km/s, shown by the stripe in the density–velocity diagram, Fig. 7). When the  $C_w$ -value is increased in solution R8, the modeled and observed gravity field show good agreement, and there is a minimal scattering of data points in the velocity–density diagram. Therefore, this solution is considered optimal. In solution R9, at a high  $C_w$ -value, an ideal velocity–density relation is obtained, but the gravity field fit worsens ( $\delta g$  in Table 4). The gravity fit of the outline of the local anomalies gets poorer in some places with increasing  $C_w$ -value (e.g. the Santa Catalina Ridge), but in other places the gravity fit is independent of the  $C_w$ -value (e.g. between the Patton accretionary belt and the San Clemente ridge).

In solution R8 (Fig. 8), where  $b = 0.390$ , the density model shows no essential mantle heterogeneities under the Borderland, and the low density body under the Santa Catalina ridge is more pronounced than in solution R5 with the local isostatic imbalance in the inner part of the mantle up to  $\sim -0.7$  kbar. The average density of the consolidated crust onshore is smaller than in solution R5 (Fig. 5).

#### 4.4. Solution R10–R16

In this set of solutions, we fix the  $b$ -coefficients at values ranging from 0.1 to 0.6 to test which  $b$ -values destroy the gravity fit. The densities, both in the crust and the mantle, are allowed to vary within the limits shown in Table 3. We chose a  $C_p$ -value of  $10^6$  to assure isostatic balance and a  $C_w$ -value of  $10^9$  to achieve an approximate linear velocity–density relation. Analysis of these solutions shows extremely high ambiguity of the mantle density definition. Solution R11, with  $b = 0.1$  (Fig. 9), and R16, with  $b = 0.6$  (Fig. 10), both show dramatic differences in mantle and crustal densities, and in the inner isostatic imbalance, while producing practically the same gravity curves. Solutions with higher  $b$ -coefficients than 0.5 require that the lower Mojave consolidated crust (Fig. 11) has an extremely low average density of  $\sim 2.72$  g/cm<sup>3</sup>, and imply the absence of a basaltic layer and high silica content in the rocks for the entire crust (average density of the whole crust  $\sim 2.75$  g/cm<sup>3</sup>). Solutions with a low  $b$ -value ( $< 0.2$ ) require that the lower crust of the Mojave Desert has a density of  $\sim 2.89$  g/cm<sup>3</sup> and a consolidated average density of  $\sim 2.78$  g/cm<sup>3</sup>, signifying a mostly basaltic lower crust and an intermediate average crustal composition. The variant with mostly granitic–gneissic average crust is preferred based on results of previous studies. On all long-range whole crustal models crossing the San Andreas fault, the average density of the Mojave crust is always lower than the crust on the Borderland side of the San Andreas fault (Li et al., 1992b; Malin et al., 1995; Kohler, 1999; Langenheim, 1999). Also Zhu and Kanamori (2000) derive an average  $V_p/V_s$ -ratio of 1.78 ( $\pm 0.27$ ) for southern California with a lower ratio in the Mojave Desert, implying mostly felsic, and therefore lighter, crust.

#### 4.5. Isostatic analysis

For all models, the isostatic balance is better for LARSE-2 profiles than for LARSE-1 profiles. On the LARSE-2 profiles, the first supplementary isostatic compensation level is always located near the Moho boundary, suggesting that the “Airy” scheme works rather well. On LARSE-1 profiles, the area beneath the San Gabriel Mountains is always anomalous in the sense of “Airy” isostasy. In our model with minimal mantle density variations (Fig. 9a), a local

---

Fig. 12. A hypothetical and simplified scheme of the possible tectonic evolution of lithospheric downwelling beneath the Transverse Ranges. (a) Initial stage. A transposition on the San Andreas fault caused a gravity instability at the lithosphere/asthenosphere boundary and the downwelling of the more dense lithosphere into the asthenosphere began. (b) The lithosphere beneath the Peninsular Ranges decoupled from the crust, and the movement of the lithosphere weakly affects the crust. However, beneath the Mojave Province, lithospheric drag captures and pulls some parts of the lower basaltic layer. This results in erosion of the basaltic layer from beneath the Mojave block and an asymmetrical lithospheric downwelling. (c) Downgoing basaltic fragments transform to eclogites. Concurrent with lithospheric downwelling, asthenospheric hot material is replaced. (d) The present-day situation. The lower basaltic layer from beneath the Mohave block has almost been eroded. Downgoing high-density material is surrounded by hot asthenospheric material. Compression is caused by formation of the crust complex, mostly in the Peninsular Ranges (San Gabriel mountains), and also by minor thrusting in the Mojave block. A crustal root is centered beneath the locus of deformation in the crust.

isostatic compensation of the topography of the San Gabriel Mountains is not reached at any level, while at higher  $b$ -values (Figs. 8a and 10a), local compensation of the topography is reached at levels of 80–100 km. This is an argument for higher ( $b > 0.3$ )  $b$ -values.

At increasing  $b$ -values, however, the total isostatic imbalance of the models becomes unrealistically large. In solution R16 (Fig. 10) with the highest  $b$ -values (0.6), the total isostatic imbalance reaches 2.5 kbar on the LARSE-1 profile inside the mantle (−1.0 kbar beneath Santa Catalina Ridge, and 1.5 kbar at the bottom of the model beneath the San Gabriel Mountains). With lower  $b$ -values, the imbalance becomes smaller and more realistic (Fig. 9). The imbalance remains high at  $b = 0.4$  (about 2.0 kbar in total, including −0.7 kbar beneath the Santa Catalina Ridge, and 1.3 kbar at the bottom of the model beneath the San Gabriel Mountains). This implies that the optimal  $b$ -value should be around (0.2–0.4).

## 5. Conclusions

1. Our modeling shows that it is possible to construct many density models that fit the observed gravity ( $\delta g < 9$  mGal), even when constrained by a linear density/velocity relation in the mantle, and isostatic compensation for the “normal” oceanic and continental columns ( $\delta p < 30$  bar).
2. Models with high  $b$ -coefficients (0.5–0.6) in a linear ( $\rho = a + bV$ ) estimation of the mantle velocity–density relation require that the consolidated crust of the Mojave Desert has an unusually low average density of around  $2.75 \text{ g/cm}^3$ . This implies a high silica content for rocks of the entire crust and a low density for the lower crust, which in turn suggests the absence of a basaltic layer on the whole, and only minor contributions from basic rock. The lower  $b$ -values (0–0.2) require that the Mojave block has a consolidated crust with an average density of around  $2.78 \text{ g/cm}^3$  and a density of the lower crust of around  $2.89 \text{ g/cm}^3$ , which corresponds mostly to basic rocks. However, this contradicts the results of a number of studies that indicate both a low  $V_p$  ( $\sim 6.3$  km/s) and a low  $V_p/V_s$ -ratio in the Mojave Desert, implying mostly felsic rocks.
3. The analysis of the isostatic imbalance of the models suggests an optimal  $b$ -value in the linear velocity–density relation ( $\rho = a + bV$ ) within the interval of (0.2–0.4).
4. Taking into account the results of our density modeling, as well as all direct and indirect evidence, solutions with  $b$ -values of  $\sim 0.2$ –0.4 are considered to be optimal. Although each argument is not strong enough on its own to completely exclude other possibilities with lower or higher  $b$  coefficients, considered together they do constrain a preferred model.
5. The density–seismic velocity relation for the preferred density model implies that both thermal and moderate petrological effects occur inside the downwelling of the uppermost mantle high velocity body beneath the Transverse Ranges. Together with other structural tectonic features of southern California, this allows us to outline some of the features of the tectonic evolution of the downwelling flow (Fig. 12). There is no data to indicate the capture of crustal material from beneath the Borderland side of the San Andreas fault by the downwelling flow. However, the lower layer of the Mojave crust is characterized by an extremely exhausted lower crust, with only a minor basaltic component. This allow us to propose that initial Mojave crust contained a basaltic layer and was thicker (up to 40 km thick, assuming the standard crust of the Precambrian platforms and cratons (Christensen and Mooney, 1995)). However, the downwelling of the lithosphere mantle beneath the San Andreas fault has pulled down most of the basaltic layer from beneath the Mojave Province, at least from beneath the part that is crossed by our modeling profiles. These captured basaltic inclusions may have transformed into eclogites. The transformation is accompanied by a considerable increase in seismic velocities and densities. Because the volume of basaltic inclusions is small compared to hosted mantle rocks, we observe a moderate increase of  $b$  coefficients in the linear bulk density–velocity relation.

## Acknowledgments

The authors thank G.S. Fuis, V.E. Langenheim and R.G. Bohannon for kindly making the original data available. The authors also thank G.S. Fuis, R.J. Blakely, N. Okaya and many others for their help and discussions. We are very grateful to reviewers R. Keller and M. Bielik for their very careful reading of the text and very insightful criticisms and comments. This work was partly supported under RFBI N 04-05-65092 and N 07-05-001069.

### Appendix A. Gravity inversion method

The modeling approach is based upon Strakhov and Romanyuk (1984), Romanyuk (1993), and Romanyuk et al. (2001, 2003) and solves the linear gravimetric inverse problem with Tikhonov’s regularization (Tikhonov and Arsenin, 1979). To apply this approach, the cross-sections are divided into blocks, each with constant density  $\rho_m$  (Fig. A.1(b)). The entire density model can then be described by a set of densities represented by a vector  $\vec{\rho} = \{\rho_m\}$ , where  $m = 1, \dots, M$  and  $M$  is the number of density blocks ( $M = 283$ ). The top boundary of the model is given by the relief (Fig. A.1(b)).

In the applied method, three quadratic functions having a certain physical meaning are compiled:

1. The function  $G(\vec{\rho}, G_0)$  is the least square discrepancy between the observed  $g_k^{obs}$  and modeled  $g_k^{mod}(\vec{\rho})$  gravity field at the location, and is given by:

$$G(\vec{\rho}, G_0) = \sum_{k=1}^K [g_k^{mod}(\vec{\rho}) - g_k^{obs} - G_0]^2, \quad \delta g = \sqrt{\frac{G(\vec{\rho}, G_0)}{K}} \tag{A.1}$$

where  $k = 1, \dots, K$ , and  $K$  is the number of points along the gravity profiles ( $K_1 = 1845, K_2 = 1113$ ) (Fig. 4(a)). The modeled gravity field,  $g_k^{mod}(\vec{\rho})$ , is calculated according to Strakhov et al. (1986a, 1986b). The constant  $G_0$  adjusts

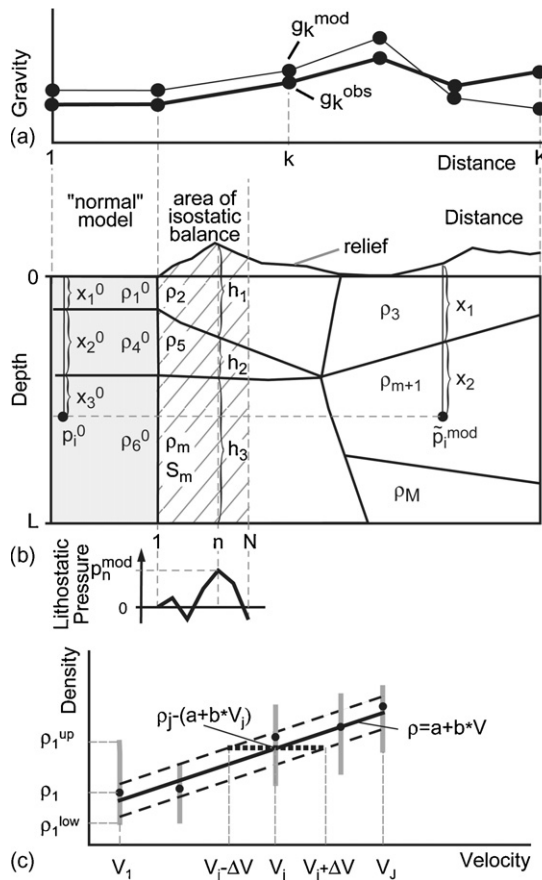


Fig. A.1. Schematic illustration to explain the theoretical modeling approach. (a) Schematic gravity profile showing the definition of observed  $g_k^{obs}$  and modeled  $g_k^{mod}(\vec{\rho})$  gravity points used in Eq. (A.1). (b) Schematic density cross-section illustrating the variables and parameter definitions used in the pressure calculations, i.e. Eqs. (A.2), (A.2a), (A.2b), (1), (1a) and (1b). (c) Velocity–density diagram. Each point in the diagram corresponds to a single density block of the cross-section. The linear approximation  $\rho = a + bV$  is shown by the thick solid lines, while the dashed lines mark the stripe (band) of  $\pm \Delta V$  which is the standard error of velocity determination in the upper mantle. Gray bars correspond to allowed density range variations, i.e.  $\rho_m^{low} < \rho_m < \rho_m^{up}$  in relation (A.5).

the model to the observed absolute gravity level, and allows us to use absolute density values. The standard deviation of the gravity field, describing the divergence of the modeled and observed gravity field, is given by  $\delta g$ .

2. The function  $P(\vec{\rho})$  reflects the degree of isostatic imbalance of the indicated parts of the model at the indicated level. It is the least squares discrepancy of the lithostatic relative pressure,  $p_n^{\text{mod}}(\vec{\rho})$ , at point  $n$  at the bottom of the model (Fig. A.1(b)), and the mean pressure of the model,  $\rho_0 L$ , at depth  $L$  of isostatic compensation ( $L = 200$  km), and is given by:

$$P(\vec{\rho}) = \sum_{n=1}^N [p_n^{\text{mod}}(\vec{\rho}) - L\rho_0]^2, \quad \delta p = \sqrt{\frac{P(\vec{\rho})}{N}} \quad (\text{A.2})$$

where  $n = 1, \dots, N$ , and  $N$  is the number of points along the pressure profile ( $N = 40$ ), and  $\rho_0$  is the average density of the area over which the hydrostatic pressure is calculated. The principle for the calculation of  $p_n^{\text{mod}}(\vec{\rho})$  and  $\rho_0$  is illustrated in Fig. A.1(b) and is given by:

$$p_n^{\text{mod}}(\vec{\rho}) = h_1\rho_2 + h_2\rho_5 + h_3\rho_m \quad (\text{A.2a})$$

$$\rho_0 = \frac{S_2\rho_2 + S_5\rho_5 + S_m\rho_m}{S_2 + S_5 + S_m} \quad (\text{A.2b})$$

where  $\rho_i$  is the density,  $h_i$  the height, and  $S_m$  is the area of the density block. The standard deviation of the isostatic pressure, describing the divergence from isostatic balance, is given by  $\delta p$ .

3. The function  $W(\vec{\rho}, a, b)$  describes the degree of scattering of the mantle densities  $\rho_j$  around the linear relation  $\rho = a + bV$ , and is given by:

$$W(\vec{\rho}, a, b) = \sum_{j=1}^J [\rho_j - (a + bV_j)]^2 \quad (\text{A.3})$$

where  $V_j$  is the seismic P-wave velocity, and  $\rho_j$  is the density, with  $j = 1, \dots, J$ , and  $J$  is the number of mantle blocks included in this relation ( $j = 38(\text{LARSE-1}) + 35(\text{LARSE-2})$ ) (Fig. 4(c)). With less scattering, the value of the function  $W(\vec{\rho}, a, b)$  becomes smaller.

To build a solution that is isostatically balanced and shows a linear velocity–density correlation in the mantle, the summary function  $F(\vec{\rho}, G_0, a, b)$  is assembled:

$$F(\vec{\rho}, G_0, a, b) = G(\vec{\rho}, G_0) + C_p P(\vec{\rho}) + C_w W(\vec{\rho}, a, b) = \min \quad (\text{A.4})$$

where  $P(\vec{\rho})$  and  $W(\vec{\rho}, a, b)$  are included with their own weighting coefficients  $C_p$  and  $C_w$  (regularization parameters). When  $C_p = C_w = 0$ , the regularizations are excluded from Eq. (A.4), and an ordinary linear gravity inversion is carried out. In this case, the solution satisfies the observed gravity field, i.e. the discrepancy  $\delta g$  (Eq. (A.1)) is minimal. However, the pressure discrepancy,  $\delta p$  (Eq. (A.2)), may be large, and velocity–density points may be distributed chaotically in the velocity–density diagram with no linear correlation. If values of  $C_p$  and  $C_w$  are increased, the contributions of functions  $P(\vec{\rho})$  and  $W(\vec{\rho}, a, b)$  in the summary function  $F(\vec{\rho}, G_0, a, b)$  increase. Hence, the isostatic equilibrium of the model and the linear velocity–density correlation begin to improve. However, this could result in a worsening of the gravity fit.

Solutions are obtained by minimizing the function  $F(\vec{\rho}, G_0, a, b)$  using the algorithm of conjugate gradients with *a priori* constraints given by fixed lower (low) and upper (up) limits for all variables (Polyak, 1969), i.e.:

$$\rho_m^{\text{low}} < \rho_m < \rho_m^{\text{up}}, \quad G_0^{\text{low}} < G_0 < G_0^{\text{up}}, \quad a^{\text{low}} < a < a^{\text{up}}, \quad b^{\text{low}} < b < b^{\text{up}} \quad (\text{A.5})$$

All variables are determined during the inversion.

## References

- Anderson, D.L., Bass, J.D., 1984. Mineralogy and composition of the upper mantle. *Geophys. Res. Lett.* 11, 637–640.
- Baheer, S., 2004. Crustal structure from San Clemente Island to the Mojave Desert in southern California; results from Los Angeles Region Seismic Experiment: Phase I. *Seis. Res. Lett.* 75 (2), 261.

- Billen, M.I., Houseman, G.A., 2004. Lithospheric instability in obliquely convergent margins: San Gabriel Mountains, southern California. *J. Geophys. Res.* 109, B01404, doi:10.1029/2003JB002605.
- Birch, F., 1961. Composition of the Earth's mantle. *Geophys. J. R. Astronom. Soc.* 4, 295–311.
- Bohannon, R.G., Gardner, J.V., Sliter, R.W., 2004. Holocene to Pliocene tectonic evolution of the region offshore of the Los Angeles urban corridor, southern California. *Tectonics* 23, TC1016.
- Bohannon, R.G., Geist, E., 1998. Upper crustal structure and Neogene tectonic development of the California continental borderland. *GSA Bull.* 110 (N6), 779–800.
- Brocher, T.M., Ruebel, A.L., Wright, T.L., Okaya, D., 1998. Compilation of 20 sonic and density logs from 12 oil test wells along LARSE lines 1 and 2, Los Angeles region, California, U.S. Geol. Survey Open File Rep., 98–366, 53pp.
- Brocher, T.M., ten Brink, U.S., Abramovitz, T., 1999. Synthesis of crustal seismic structure argues against a slab gap beneath coastal California. *Int. Geol. Rev.* 41, 263–274.
- Carena, S., Suppe, J., 2002. Three-dimensional imaging of active structures using earthquake aftershocks: the Northridge thrust, California. *J. Struct. Geol.* 24, 887–904.
- Carlson, R.L., Raskin, G.S., 1984. Density of the ocean crust. *Nature* 311, 555–558.
- Cheadle, M.J., Czuchra, B.L., Byrne, T., Ando, C.J., Oliver, J.E., Brown, L.D., Kaufman, S., 1986. The deep crustal structure of the Mojave Desert, California, from COCORP seismic reflection data. *Tectonics* 5, 293–320.
- Christensen, N.I., Mooney, W.D., 1995. Structure and composition of the continental crust: a global view. *J. Geophys. Res.* 100 (B7), 9761–9788.
- Constenius, K.N., Johnson, R.A., Dickinson, W.R., Williams, T.A., 2000. Tectonic evolution of the Jurassic-Cretaceous Great Valley forearc, California: implications for the Franciscan thrust-wedge hypothesis. *GSA Bull.* 112 (N11), 1703–1723.
- Davis, T.L., Namson, J.S., 1994. A balanced cross-section of the 1994 Northridge earthquake, southern California. *Nature* 372, 167–169.
- Dokka, R.K., 1989. The Mojave extensional belt of southern California. *Tectonics* 8, 363–390.
- Duffy, T.S., Anderson, D.L., 1989. Seismic velocities in mantle minerals and the mineralogy of upper mantle. *J. Geophys. Res.* 94, 1895–1912.
- Ehlig, P.L., 1981. Origin and tectonic history of the basement terrain of the San Gabriel Mountains, central Transverse Ranges. In: Ernst, W.G. (Ed.), *The Geotectonic Development of California*. Prentice-Hall, Englewood Cliffs, NJ, pp. 253–283.
- Fisher, M.A., Normark, W.R., Langenheim, V.E., Calvert, A.J., Sliter, R., 2003. Geology of the continental margin beneath Santa Monica Bay, southern California, from seismic-reflection data. *Bull. Seis. Soc. Am.* 93 (5), 1955–1983.
- Fuis, G.S., 1998. West margin of North America—a synthesis of recent seismic transects. *Tectonophysics* 288, 265–292.
- Fuis, G.S., Ryberg, T., Godfrey, N.I., Okaya, D.A., Murphy, J.M., 2001. Crustal structure and tectonics from the Los Angeles basin to the Mojave Desert, southern California. *Geology* 29, 15–18.
- Fuis, G.S., Clayton, R.W., Davis, P.M., Ryberg, T., Lutter, W.J., Okaya, D.A., Hauksson, E., Prodehl, C., Murphy, J.M., Benthien, M.L., Baher, S.A., Kohler, M.D., Thygesen, K., Simila, G., Keller, G.R., 2003. Fault systems of the 1971 San Fernando and 1994 Northridge earthquakes, southern California: Relocated aftershocks and seismic images from LARSE II. *Geology* 31, 171–174.
- Fuis, G.S., Baher, S., Murphy, J.M., Langenheim, V.E., Howard, K.A., Catchings, R.D., Fisher, M.A., Matti, J.C., Okaya, D.A., Henyey, T.L., Clayton, R.W., Davis, P.M., Nicholson, C., Oskin, M., 2004. The proposed southern California Imaging Project (SCIP); targeting structure of the Transverse Ranges. *Seis. Res. Lett.* 75 (2), 258–259.
- Glazner, A.F., Farmer, G.L., Hughes, W.T., 1991. Contamination of Basaltic magma by mafic crust at Amboy and Pisgah Craters, Mojave Desert, California. *J. Geophys. Res.* 96 (NB8), 13673–13691.
- Glazner, A.F., Bartley, J.M., Sanner, W.K., 2000. Nature of the southwestern boundary of the central Mojave Tertiary province, Rodman Mountains, California. *GSA Bull.* 112 (N1), 34–44.
- Godfrey, N., Beaudoin, B.C., Klemperer, S.L., Levander, A.R., Luetgert, J.H., Meltzer, A.S., Mooney, W.D., Trehu, A.M., 1997. Ophiolitic basement to the Great Valley forearc basin, California, from seismic and gravity data, implications for crustal growth at the North American continental margin. *GSA Bull.* 109 (N12), 1536–1562.
- Godfrey, N., Klemperer, S., 1998. Ophiolitic basement to a forearc basin and implications for continental growth; the Coastal Range/Great Valley Ophiolite, California. *Tectonics* 17 (N4), 558–570.
- Godfrey, N.J., Fuis, G.S., Langenheim, V., Okaya, D.A., 2002. Lower crustal deformation beneath the central Transverse Ranges, southern California: results from the Los Angeles region seismic experiment. *J. Geophys. Res.* 107 (B7), ETG1–ETG19.
- Hadley, D., Kanamori, H., 1997. Seismic structure of the Transverse Ranges, California. *Geol. Soc. Am. Bull.* 88, 1469–1478.
- Hauksson, E., 2000. Crustal structure and seismicity distribution adjacent to the Pacific and North America boundary in southern California. *J. Geophys. Res.* 105, 13875–13903.
- Hauksson, E., Haase, J.S., 1997. Three-dimensional  $V_p$  and  $V_p/V_s$  velocity models of the Los Angeles basin and central Transverse Ranges, California. *J. Geophys. Res.* 102, 5423–5453.
- Hook, S.J., Karlstrom, K.E., Miller, C.F., McCaffrey, K.J.W., 1994. Mapping the Piute Mountains, California, with thermal infrared multispectral scanner (TIMS) images. *J. Geophys. Res.* 99, 15605–15622.
- Houseman, G.A., Neil, E.A., Kohler, M.D., 2000. Lithosphere instability beneath the Transverse Ranges of California. *J. Geophys. Res.* 105, 16237–16250.
- Huftile, G.J., Yeats, R.S., 1995. Convergence rates across a displacement transfer zone in the western Transverse Ranges, Ventura basin, California. *J. Geophys. Res.* 100, 2043–2067.
- Humphreys, E., Clayton, R.W., Hager, B.H., 1984. A tomographic image of mantle structure beneath southern California. *Geophys. Res. Lett.* 11, 625–627.
- Humphreys, E., Clayton, R.W., 1990. Tomographic image of the southern California Mantle. *J. Geophys. Res.* 95, 19725–19746.
- Humphreys, E., Hager, B.H., 1990. A kinematic model for the late Cenozoic development of southern California. *J. Geophys. Res.* 95, 19,747–19,762.

- Jachens, R.C., Griscom, A., 1985. An isostatic residual gravity map of California—a residual map for interpretation of anomalies from intracrustal sources. In: Hinze, W.J. (Ed.), *The Utility of Regional Gravity and Magnetic Anomaly Maps*. Society of Exploration Geophysics, Tulsa, OK, pp. 347–360.
- Jordan, T.H., 1978. Composition and development of the continental tectonosphere. *Nature* 274, 544–548.
- Jordan, T.H., 1981. Continents as a chemical boundary layer. *Philos. Trans. R. Soc. Lond. Ser. A* 301, 359–373.
- Keller, B., Prothero, W., 1987. Western transverse ranges crustal structure. *J. Geophys. Res.* 92, 7890–7906.
- Kenney, M., Weldon, R., 1998. Geologic Map; Mescal Creek 7.5-minute quadrangal, northeastern San Gabriel Mountains, southern California [abs]. *GSA Bull.* 30 (N5), 23.
- Kohler, M.D., Davis, P.M., 1997. Crustal thickness variations in southern California from Los Angeles region seismic experiment passive phase teleseismic travel times. *Bull. Seismol. Soc. Am* 87, 1330–1344.
- Kohler, M.D., 1999. Lithospheric deformation beneath the San Gabriel Mountains in the southern California Transverse Range. *J. Geophys. Res.* 104, 15,025–15,041.
- Langenheim, V.E., 1999. Gravity and Aeromagnetic Models along the Los Angeles Region Seismic Experiment (Line 1), California, U.S. Geol. Survey Open File Rep., 99–388, 22 pp.
- Langenheim, V.E., Jachens, R.C., 1996. Gravity data collected along the Los Angeles Regional Seismic Experiment (LARSE) and preliminary model of regional density variations in basement rocks, southern California, U.S. Geol. Survey Open File Rep., 96–682, 25 pp.
- Langenheim, V.E., Hauksson, E., 2001. Comparison between crustal density and velocity variations in southern California. *Geophys. Res. Lett.* 28 (N16), 3087–3090.
- Langenheim, V.E., Griskom, A., Jachens, R.C., Hildenbrand, T.G., 2000. Preliminary potential-field constraints on the geometry of the San Fernando Basin, southern California, Open file report 00-219, USGS, Menlo Park, 36 pp.
- Langenheim, V.E., Jachens, R.C., Morton, D.M., Kistler, R.W., Matti, J.C., 2004. Geophysical and isotopic mapping of preexisting crustal structures that influenced the location and development of the San Jacinto fault zone, southern California. *Geol. Soc. Am. Bull.* 116 (9–10), 1143–1157.
- Li, Y.-G., Henyey, T.L., Silver, L.T., 1992a. Aspects of the crustal structure of the Western Mojave Desert, California, from seismic reflection and gravity data. *J. Geophys. Res.* 97, 8805–8816.
- Li, Y.-G., Henyey, T.L., Leary, P.C., 1992b. Seismic reflection constraints on the structure of the crust beneath the San Bernardino Mountains, Transverse Ranges, southern California. *J. Geophys. Res.* 97, 8817–8830.
- Li, Y.-G., Henyey, T.L., Okaya, D., Davis, P., Day, S.M., Bohannon, R.G., 1993. Offshore-to-onshore seismic Recording in the southern California Borderlands—Peninsular Ranges [abs.]. *Eos. Trans. Am. Geophys. Union* 74, 445.
- Lutter, W.J., Fuis, G.S., Thurber, C.H., Murphy, J., 1999. Tomographic images of the upper crust from the Los Angeles basin to the Mojave Desert, California: results from the Los Angeles region seismic experiment. *J. Geophys. Res.* 104, 25,543–25,565.
- Lutter, W.J., Fuis, G.S., Ryberg, T., Okaya, D.A., Clayton, R.W., Davis, P.M., Prodehl, C., Murphy, J.M., Benthien, M.L., Godfrey, N.J., Christensen, N.I., Thygesen, K., Thurber, C.H., Simila, G., Keller, G.R., Langenheim, V., 2004. Upper crust structure from the Santa Monica Mountains to the Sierra Nevada, southern California: Tomographic results of the Los Angeles Regional Seismic Experiment, Phase 2 (LARSE II). *Bull. Seis. Soc. Am.* 94 (2), 619–632.
- Magistrale, H., 2002. Relative contributions of crustal temperature and composition to controlling the depth of earthquakes in southern California. *Geophys. Res. Lett.* 29, 10, doi:10.1029/2001GL014375.
- Magistrale, H., Zhou, H.-W., 1996. Lithological control of the depth of earthquakes in southern California. *Science* 273, 639–642.
- Malin, P.E., Goodman, E.D., Henyey, T.L., Li, Y.G., Okaya, D.A., Saleeby, J.B., 1995. Significance of seismic reflection beneath a tilted exposure of deep continental crust, Tehachapi Mountains, California. *J. Geophys. Res.* 100, 2069–2087.
- McCaffree Pellerin, C.L., Christensen, N.I., 1998. Interpretation of crustal seismic velocities in the San Gabriel—Mojave region, southern California. *Tectonophysics* 286, 253–271.
- McCulloh, T.H., 1960. Gravity variations and the geology of the Los Angeles basin of California, U.S. Geol. Survey Prof. Paper, 400-B, pp. 320–325.
- Miller, J.S., Glazner, A.F., Farmer, G.L., Suayah, G.L., Suayah, I.B., Keit, L.A., 2000. A Sr, Nd, and Pb isotopic study of mantle domains and crustal structure from Miocene volcanic rocks in the Mojave Desert, California. *Geol. Soc. Am. Bull.* 112, 1264–1279.
- Miller, K.C., 2002. Geophysical evidence for Miocene extension and mafic magmatic addition in the California Continental Borderland. *GSA Bulletin*, v.114 (N4), 499–512.
- Nazareth, J.J., Clayton, R.W., 2003. Crustal structure of the Borderland–continent transition zone of southern California adjacent to Los Angeles. *J. Geophys. Res.* 108 (B8), 2404, doi:10.1029/2001JB000223.
- Pysklywec, R.N., Beamont, C., Fullsack, P., 2000. Modeling the behavior of the continental mantle lithosphere during plate convergence. *Geology* 28, 655–658.
- Politz, F.F., Peltzer, G., Burgmann, R., 2000. Mobility of continental mantle: Evidence from postseismic geodetic observations following the 1992 Landers earthquake. *J. Geophys. Res.* 105, 8035–8054.
- Polyak, B.T., 1969. The method of conjugate gradients in extreme problems. *J. Calculat. Math. Math. Phys.* 9, 807–821.
- Raith, R., Shor, G., Francis, T., Morris, G., 1969. Anisotropy of the Pacific upper mantle. *J. Geophys. Res.* 74, 3095–3109.
- Richards-Dinger, K.B., Shearer, P.M., 1997. Estimating crustal thickness in southern California by stacking PmP arrivals. *J. Geophys. Res.* 102, 15,211–15,224.
- Romanyuk, T.V., 1993. The method of gravity inversion: application to density modeling of the lithosphere along the Angola-Brazil geotraverse. In: Montag, H., Reigber, C. (Eds.), *Geodesy, Physics of the Earth*. IAG Symposium Series. Springer, pp. 252–255.
- Romanyuk, T.V., Mooney, W.D., Blakely, R.J., 2001. Density model of the Cascadia Subduction Zone, *Izvestiya. Phys. Solid Earth* 37 (8), 617–635.
- Romanyuk, T.V., Mooney, W.D., Detweiler, S., 2003. Models of the density distribution in the lithosphere across the San Andreas Fault, southern California, *Izvestiya. Phys. Solid Earth* 39 (5), 365–391.

- Ryberg, T., Fuis, G., 1998. The San Gabriel Mountains bright reflective zone: possible evidence of young mid-crustal thrust faulting in southern California. *Tectonophysics* 286, 31–46.
- Sato, H., Sacks, E., Takahashi, E., Scarfe, C.M., 1988. Geotherms in the Pacific Ocean from laboratory and seismic attenuation studies. *Nature* 336, 154–156.
- Sato, H., Sacks, I.S., Murase, T., Muncill, G., Funkuyama, H., 1989. Qp-melting temperature relation in peridotite at high pressure and temperature: Attenuation mechanism and implications for the mechanical properties of the upper mantle. *J. Geophys. Res.* 94 (8), 10,647–10,661.
- Sato, H., Sacks, I.S., 1989. Anelasticity and thermal structure of the oceanic mantle: temperature calibration with heat flow data. *J. Geophys. Res.* 94 (5), 5705–5715.
- Shaw, J.H., Shearer, P.M., 1999. An elusive blind-thrust fault beneath metropolitan Los Angeles. *Science* 283, 1516–1518.
- Sheffels, B., McNutt, M., 1986. Role of subsurface loads and regional compensation in the isostatic balance of the Transverse Ranges, California: evidence for intracontinental subduction. *J. Geophys. Res.* 91, 6419–6431.
- Sheffels, B., McNutt, M., 1987. Correction to “role of subsurface loads and regional compensation in the isostatic balance of the Transverse Ranges, California: evidence for Intracontinental Subduction”. *J. Geophys. Res.* 97, 6444.
- Shor, G., Raitt, R., 1958. Seismic studies in the Southern California Continental Borderland, International Geological Congress, Mexico City, Section 9, pp. 243–258.
- Silver, L.T., James, E.W., 1988. Geological setting and lithologic column of the Cajon Pass deep drillhole. *Geophys. Res. Lett.* 15, 941–944.
- Strakhov, V.N., Romanyuk, T.V., 1984. Determination of crustal and upper mantle densities from DSS and gravity data, I, II: *Izvestiya AN SSSR. Fizika Zemli* N6, 44–80.
- Strakhov, V.N., Lapina, M.I., Efimov, A.V., 1986a. A Solution to forward problems in gravity and magnetism with new analytical expressions for the field elements of standard approximating bodies. I: *Izvestiya. Earth Phys.* 22 (N6), 471–482.
- Strakhov, V.N., Lapina, M.I., Efimov, A.V., 1986b. A solution of direct gravity and magnetic problems with new analytical expressions of the field elements of typical approximating bodies. II: *Izvestiya. Earth Phys.* 22 (N7), 566–575.
- Sung, L., Jackson, D.D., 1992. Crustal and uppermost mantle structure under southern California. *Bull. Seismol. Soc. Am* 82, 934–961.
- ten Brink, U.S., Zhang, J., Brocher, T.M., Okaya, D.A., Klitgord, K.D., Fuis, G.S., 2000. Geophysical evidence for the evolution of the California Inner Continental Borderland as a metamorphic core complex. *J. Geophys. Res.* 105, 5835–5857.
- Tsutsumi, H., Yeats, R.S., 1999. Tectonic setting of the 1971 Sylmar and 1994 Northridge Earthquakes in San Fernando Valley, California. *Bull. Seis. Soc. Am.* 89 (N5), 1232–1249.
- Tikhonov, A.N., Arsenin, V., 1979. *The Methods of Solution of Ill-posed Problems*. Nauka, Moscow, 284 pp (in Russian).
- Vedder, J.G., Crouch, J.K., Lee-Wong, F., 1981. Comparative study of rocks from deep sea drilling project holes 467, 468 and 469 and the southern California Borderland, In: Yeats, R.S., Haq, B.U., et al. (Eds.), *Init. Repts. DSDP, 63*. Washington (U.S. Govt. Printing Office), pp. 907–917.
- Walker, J.D., Fletcher, J.M., Fillmore, R.P., Martin, M.W., Taylor, W.J., Glazner, A.F., Bartley, J.M., 1995. Connection between igneous activity and extension in the central Mojave metamorphic core complex, California. *J. Geophys. Res.* 100, 10,477–10,494.
- Wooley, R.J., Langenheim, V.E., 2001. Gravity data along LARSE (Los Angeles Regional Seismic Experiment) Line II, southern California, Open file report 01-375, USGS, Menlo Park, 22 pp.
- Wright, T.L., 1991. Structural, geology and tectonic evolution of the Los Angeles Basin, California. In: Biddle, K.T. (Ed.), *Active Margin Basins*, vol. 52. *Am. Assoc. Pet. Geol. Mem.*, pp. 35–134.
- Wright, T.L., Yeats, R.S. (Eds.), 1997. *Geology and Tectonics of the San Fernando Valley and East Ventura Basin*. *Am. Assoc. Petr. Geol., Pacific Section*, p. GB77.
- Yeats, R.S., Haq, B.U., and Pisciotto, K.A., 1981. Introduction and explanatory notes, deep sea drilling project LEG 63, In: Yeats, R.S., Haq, B.U., et al., *Init. Repts. DSDP, 63*: Washington (U.S. Govt. Printing Office), 5-412.
- Yeats, R.S., and Haq, B.U., 1981. Deep-sea drilling off the Californias: Implications of LEG 63, In: Orlofsky, S. [Ed.] *Init. Reports DSDP, 63*: Washington (U.S. Govt. Printing Office), 949-962.
- Yeats, R.S., Huftile, G.J., 1995. The Oak Ridge fault system and the 1994 Northridge earthquake. *Nature* 273, 418–421.
- Zhao, D., Kanamori, H., Humphreys, E., 1996. Simultaneous inversion of local and teleseismic data for the crust and mantle structure of southern California. *Phys. Earth Planet. Int.* 93, 191–214.
- Zhu, L., 2000. Crustal structure across the San Andreas Fault, southern California from teleseismic converted waves. *Earth Planet. Sci. Lett.* 179, 183–190.
- Zhu, L., Kanamori, H., 2000. Moho depth variation in southern California from teleseismic receiver functions. *J. Geophys. Res.* 105, 2969–2980.